

05/04/2012

1 **MIOCENE ANDALUSITE LEUCOGRANITE IN CENTRAL-EAST HIMALAYA**  
2 **(EVEREST-MASANG KANG AREA): LOW-PRESSURE MELTING DURING HEATING**

3 *Dario VISONA*<sup>a</sup>, *Rodolfo CAROSI*<sup>b</sup>, *Chiara MONTOMOLI*<sup>c</sup>, *Massimo TIEPOLO*<sup>d</sup> and  
4 *Luca PERUZZO*<sup>e</sup>

5 a Dipartimento di Geoscienze, University of Padova, Padova, Italy. [dario.visona@unipd.it](mailto:dario.visona@unipd.it)

6 b Dipartimento di Scienze della Terra, University of Torino, Torino, Italy. [carosi@unito.it](mailto:carosi@unito.it)

7 c Dipartimento di Scienze della Terra, University of Pisa, Pisa, Italy. [montomoli@dst.unipi.it](mailto:montomoli@dst.unipi.it)

8 d C.N.R.-Istituto di Geoscienze e Georisorse. UOS Pavia, via Ferrata 1 27100 Pavia, Italy. [tiepolo@crystal.unipv.it](mailto:tiepolo@crystal.unipv.it)

9 e C.N.R.-Istituto di Geoscienze e Georisorse – Sez.di Padova c/o Dip. di Geoscienze - University of Padova, Padova, Italy.  
10 [peruzzo@igg.cnr.it](mailto:peruzzo@igg.cnr.it)

11  
12 **Corresponding author:** Dario Visonà, Dipartimento di Geoscienze, University of Padova, via Gradenigo 6, I-35131 Padova, Italy.  
13 [dario.visona@unipd.it](mailto:dario.visona@unipd.it) tel. +390498279147

14  
15 **Abstract**

16 The studied Miocene andalusite-bearing leucogranites intrude the upper part of the High  
17 Himalayan Crystallines (HHC) and the north Himalayan domes and outcrop in an area stretching  
18 from Mt. Everest to the Kula Khangri massif (Bhutan) towards the east.

19 The leucogranites constitute both dykes as well as sills and parts of larger andalusite-free  
20 leucogranite plutons (e.g., Makalu). They represent mainly of two-mica (muscovite+biotite  
21 ±tourmaline±cordierite±andalusite±sillimanite±dumortierite) leucogranite, and tourmaline  
22 (muscovite+tourmaline±biotite±andalusite±sillimanite±garnet±kyanite±spinel±corundum)  
23 leucogranites. Microstructures reveal several generations of andalusite (from residual/peritectic  
24 early magmatic to cotectic late magmatic), even in the same sample. The occurrence of residual  
25 and/or peritectic andalusite, together with inclusions of sillimanite+biotite in cordierite, indicates  
26 that melts formed by dehydration melting of biotite at T = 660-700 °C during prograde heating at  
27 low-pressure conditions (P < about 400 MPa).

28 According to current models, leucogranites are produced by dehydration melting of  
29 muscovite and/or biotite during exhumation of the HHC. In this case, micas are consumed in the  
30 sillimanite stability field. As a consequence, these models cannot explain the occurrence of residual  
31 and/or peritectic magmatic andalusite. Conditions for anatexis in the andalusite field may have been  
32 achieved by heat transfer within the exhuming (extruding) HHC, from structurally lower and hotter  
33 rocks towards upper and colder fertile lithologies.

34

35

36 **Keywords:** Andalusite leucogranite; Miocene; High Himalayan Crystallines; U-Pb zircon  
37 geochronology; Petrology.

38

### 39 **1. Introduction**

40 Andalusite is a mineral found in peraluminous felsic igneous rocks, the petrological  
41 importance of which is mainly associated with its relatively limited chemical and, particularly,  
42 physical ranges of stability in melts. The composition of the source rock, degree of water saturation  
43 and alumina content of the melt are among the most important chemical factors controlling the  
44 stability of andalusite in granitic rocks (Acosta-Vigil et al., 2002, 2003; Clarke et al., 2005; Clarke  
45 et al., 2009). The essential condition for the occurrence of magmatic andalusite in granitic rocks is  
46 also that magma should have been generated or crystallised at a  $P <$  about 400 MPa (e.g. Pattison,  
47 1992). Of course andalusite may also be found in granitic rocks as a xenocrystic mineral inherited  
48 from the local country rocks but, in this case, it has no meaning for granite petrology (e.g., Clarke,  
49 2007).

50 Following many previous authors, the Himalayan leucogranites in this and other areas  
51 originated from partial melting of the crystalline basement (High Himalayan Crystallines: HHC) in  
52 response to rapid exhumation during the incongruent melting of muscovite at intermediate pressure  
53 values ( $P \sim 600$ -400 MPa,  $T \sim 700$  °C), followed by crystallisation at  $P \sim 400$  MPa (e.g. Searle et al.,  
54 2010; Streule et al., 2010; and references therein). In this framework, formation of andalusite  
55 should be limited to the final stages of crystallisation, as suggested for the Miocene leucogranite of  
56 Central Bhutan (Kellett et al., 2009). However, most of the Himalayan andalusite-bearing  
57 leucogranite described in the literature (e.g., Visonà and Lombardo, 2002; Castelli and Lombardo  
58 1988, Pognante and Benna 1993) shows textures indicating that andalusite is an early crystallisation  
59 phase. This evidence strongly suggests that the Himalayan andalusite-bearing leucogranite formed  
60 at pressures lower than those predicted by decompressional melting models (Searle et al., 2010).

61 The aim of this paper is to present and discuss the features of the Himalayan Miocene  
62 andalusite-bearing leucogranite in a larger area and in greater detail than in the previous work by  
63 Visonà and Lombardo (2002), and to explore the possibility that its formation is related to low-  
64 pressure regional heating instead of decompressional melting. The petrographic characteristics of  
65 andalusite leucogranite from the literature of the Himalayas are reviewed, and details of the  
66 petrography, mineral chemistry, minimal geochemistry and geochronology of new samples from an  
67 area east of Mt. Everest are provided. These petrographic observations are compared with those  
68 reviewed by Clarke et al. (2005) on the origin of andalusite in granites.

69

## 70 **2. Geological framework**

### 71 **2.1 The Himalaya Orogen and the Cenozoic granite belts**

72 The collision of the Indian continent with the Asia plate in the Cenozoic gave rise to the well-  
73 known Himalayan architecture, which is composed of five lithotectonic domains forming parallel  
74 belts, separated by four main tectonic lines (Gansser, 1964; Le Fort, 1975). From south to north, the  
75 Main Boundary Thrust separates Sub-Himalaya from Lower Himalaya; the Main Central Thrust  
76 separates Lower Himalaya from Higher Himalaya and, further north, the South Tibetan Detachment  
77 separates Higher Himalaya from Tibetan Himalaya. Lastly, the Indus-Tsangpo suture defines the  
78 Tibetan Plateau to the north. The Trans-Himalayan Batholith, an I-type plutonic complex originated  
79 by subduction of the oceanic crust of the Tethys Sea between 140 and 40 Ma, is located at the  
80 southern margin of the Tibetan Plateau (Fig 1).

81 Higher Himalaya is carved out of a huge thrust sheet (the Higher Himalayan Crystallines,  
82 HHC) composed of metamorphic rocks in the upper amphibolite to granulite facies and migmatites  
83 characterised by a metamorphism of Tertiary age. The HHC contains two magmatic belts consisting  
84 of S-type granite of Miocene age, the High Himalaya Granite (HHG) and North Himalayan Granite  
85 (NHG). These two belts extend from Zaskar as far as Central Bhutan and are mainly concentrated  
86 in the Central and Eastern Himalayas. The HHG forms a chain of small plutons or more commonly  
87 a network of dykes in the upper HHC (north of the High Himalayan Thrust; HHT in Fig. 1), near  
88 the South Tibetan Detachment which separates the High Himalayan Crystallines from Tibetan  
89 Himalaya. The NHG comprises a series of independent plutonic bodies intruding the gneissic dome  
90 which are considered as windows of the HHC below the Tibetan Himalaya (e.g., Larson et al.,  
91 2010; Lee et al., 2004), the sedimentary series of the pre-collision continental shelf of the India  
92 plate.

93 The HHG and NHG are generally classified as leucogranites (Debon and Le Fort, 1983)  
94 although many of these rocks have modal contents of mafic minerals exceeding 5% vol. (e.g.  
95 Visonà and Lombardo, 2002). They are peraluminous ( $ASI = 1.08-1.34$ : Debon et al., 1986; Castelli  
96 and Lombardo, 1988; Visonà and Lombardo, 2002; data reported in Acosta-Vigil et al., 2003;  
97 Zhang et al., 2004; this paper) and, according to the modal contents of tourmaline and biotite, two  
98 main types are identified (Guillot and Le Fort 1995; Dèzes, 1999; Visonà and Lombardo, 2002): i) a  
99 *two-mica* type (2mg, with tourmaline <2.6% and biotite > 1.5%), also including minor biotite  
100 granite containing scarce magmatic muscovite; ii) a less abundant *tourmaline leucogranite* (Tg,  
101 with tourmaline > 2.2% and biotite up to 1.5%). Both types may contain not only tourmaline but also  
102 other peraluminous minerals such as cordierite or, less commonly, garnet, sillimanite, andalusite,  
103 corundum, beryl, and rare xenocrystic kyanite. Both types intruded the same high structural level of

104 the HHC, and cross-cutting relationships in plutons and dyke swarms indicate in most cases that  
105 2mg intruded first and the Tg are the latest (Visonà and Lombardo, 2002, and references therein).

106

## 107 **2.2 Andalusite-bearing leucogranite**

108 Andalusite has been described in leucogranites of both granitic belts (HHG and NHG) since  
109 the early petrographic studies (Bordet, 1961; Palivcova et al., 1982; Debon et al., 1986; Pognante  
110 and Benna, 1993); it was only reported, however, in a limited number of locations. The most recent  
111 studies (Visonà and Lombardo, 2002; Rolfo et al., 2006; Kellet et al., 2009; Mosca et al., 2010)  
112 extend the areas with andalusite leucogranites to a larger sector of the central-eastern part of the  
113 Himalayan range (Figs. 1 and 2). From west to east, these occurrences are: *Gneissic domes* in the  
114 Tibetan Himalaya; *Makalu area*; *Khama-Phung Chu (Kharta)-Rongbuk area*; *Kangchenjunga and*  
115 *NE Sikkim areas*; *Central Bhutan*.

116 *The gneissic domes* in the Tibetan Himalaya are exposed by the North Himalayan antiform in  
117 southern Tibet, NE of Mount Everest. The Lagoi Kangri and Mabja-Kuday domes are intruded by  
118 two-mica granite (with biotite > muscovite) containing sillimanite, garnet, andalusite and  
119 xenocrystic kyanite (Debon et al., 1986; Zhang et al., 2004, Lee et al., 2006).

120 In the *Makalu area*, andalusite occurs in tourmaline granite and two-mica granite collected in  
121 the upper part of the Barun glacier basin, at the bottom of the West Wall of Makalu (Bordet, 1961;  
122 Pognante and Benna, 1993; Visonà and Lombardo, 2002). Andalusite two-mica granite was already  
123 described and sampled along the West Wall by Palivcova et al. (1982). The Makalu pluton is the  
124 result of the intrusion of two magmatic pulses, the first at 24-21 Ma and 15.6±0.2 Ma, respectively  
125 (Schärer et al., 1984; Streule et al., 2010). According to Streule et al. (2010), however, both pulses  
126 are composed of leucogranite with tourmaline and cordierite, and andalusite was not reported by  
127 these authors.

128 In the *Kama-Phung Chu (Kharta)-Rongbuk area* (NNE of Makalu), the HHC is intruded by  
129 numerous dykes or small subconcordant bodies of leucogranite, often with andalusite ± cordierite  
130 and/or sillimanite (Visonà and Lombardo, 2002; Cottle et al., 2009a). In most cases, these are  
131 examples of medium- to fine-grained two-mica granite, commonly containing pods or orbicules of  
132 tourmaline+quartz; tourmaline granite is less abundant and usually foliated.

133 In the *Kangchenjunga area*, the occurrence of andalusite leucogranite has been reported both  
134 on the Nepalese (Mosca et al., 2010) and Indian (Sikkim) flanks (Zemu valley; Rolfo et al., 2006).  
135 In both cases, dykes are composed of medium- to fine-grained two-mica granite with pods of  
136 tourmaline + quartz.

137 In *Central Bhutan* (SW of Kula Kangri), andalusite-bearing leucogranites have been found in  
138 sills and networks of dykes (Castelli and Lombardo, 1988; Kellet et al., 2009), commonly  
139 containing also cordierite and sillimanite.

140

### 141 3. Petrography

142 In the Everest-Sikkim area (Fig. 1), andalusite is mainly found in two-mica granite pertaining  
143 to both the NHG and HHG belts, and only to a lesser extent in tourmaline granite. Andalusite has  
144 been also found, although only once (Zemu glacier valley), as a vein mineral within the two-mica  
145 granite. The new data we present on the andalusite leucogranites of the HHG belts outcropping in  
146 the area of Fig. 2, include the scarce petrographic and geochemical data available in the literature  
147 regarding the gneissic domes of Tibetan Himalaya and Central Bhutan (Tab. 6).

148 Regarding bulk rock major element compositions, andalusite-bearing leucogranites are  
149 indistinguishable from andalusite-free leucogranites and both are classified as moderately to  
150 strongly peraluminous granites. The andalusite leucogranites have an ASI between 1.11 and 1.29  
151 (ASI = molecular ratio of  $\text{Al}_2\text{O}_3/(\text{CaO}+\text{Na}_2\text{O}+\text{K}_2\text{O})$ ; Zen 1986), are characterised by high  $\text{SiO}_2$  and  
152 low  $\text{FeO}+\text{MgO}+\text{TiO}_2$  concentrations (Tab. 6), and plot close to the minimum or eutectic melt  
153 compositions in the pseudo-ternary Qtz-Or-Ab aplogranite space (at variable  $\text{aH}_2\text{O}$  conditions and  
154 pressures between 200 and 500 MPa; Visonà and Lombardo, 2002). With the aim of ascertaining  
155 the origin of the andalusite in the Himalayan leucogranites, the following petrographic description  
156 refers to the textural and chemical criteria recently discussed by Clarke et al. (2005): *size*  
157 (compatibility or incompatibility with grain sizes of igneous minerals in the same rock), *shape*  
158 (ranging from euhedral to anhedral), and state of aggregation of andalusite (single grains, type S, or  
159 clusters of grains, type C), and its *association with muscovite* (presence or absence of  
160 monocrystalline or polycrystalline muscovite rims), and the *compositions* of coexisting minerals.  
161 Following these criteria, the three main genetic types of andalusite in felsic igneous rocks have been  
162 found in the Himalayan leucogranite: Type 1 Metamorphic (prograde and retrograde metamorphic,  
163 xenocrystic and residual), Type 2 Magmatic, and Type 3 metasomatic (Clarke et al., 2005).

164 3.1. Andalusite in leucogranites. *Andalusite tourmaline granite* occurs as medium- to coarse-  
165 grained, mostly foliated rocks, characterised by abundant muscovite and tourmaline and scarce  
166 biotite. Apatite is abundant and appears as euhedral to anhedral grains; zircon and monazite are less  
167 abundant accessories. Thin fibrous sillimanite occurs as inclusions in muscovite present in  
168 millimetric shear zones of the foliated rock. Hercynite and euhedral garnet (Spessartine:  
169  $\text{Alm}_{27}\text{Sps}_{70}\text{Andr}_3$ ) are occasionally present (Visonà and Lombardo, 2002). Sample V916 contains  
170 xenocrystic corundum (up to 3 mm in length) included in feldspar. Andalusite is commonly pink in

171 colour and its crystal size is slightly larger than that of the other rock-forming minerals (up to 8  
172 mm). Andalusite appears in single grains (S textural type, see below), fractured and deeply corroded  
173 by muscovite monocrystalline overgrowths. In some cases, euhedral andalusite is found included in  
174 tourmaline.

175 *Andalusite two-mica granite* are typically fine- to medium-grained rocks, in some cases  
176 foliated, and are located mainly in the HHG. Peraluminous minerals such as andalusite, cordierite,  
177 sillimanite and reddish-purple dumortierite are common and relatively abundant. The dumortierite  
178 grains contain plagioclase and rounded quartz, and are variably transformed into muscovite. Rare  
179 Al-spinel and relics of corundum  $\pm$  prismatic sillimanite (V731, V953) occur in plagioclase. Brown  
180 fibrous sillimanite usually fills mineral junctions in the matrix (Fig. 3a, e, f), and forms trails  
181 surrounding andalusite (when not enclosed in plagioclase; Fig. 3m). Acicular sillimanite  
182 preferentially grows on biotite borders or as fans of diverging needles in biotite and muscovite (Fig.  
183 3n). Cordierite is found as euhedral crystals, in places replaced by chlorite+muscovite, and in some  
184 samples wrapped by tourmaline. Some euhedral cordierite host relics of an older association of  
185 biotite+prismatic sillimanite, a texture interpreted as indicating magmatic-peritectic growth of  
186 cordierite during biotite melting reactions (Visonà and Lombardo, 2002). Andalusite occurs in  
187 quantities up to 5% modal (Makalu, Palivcova et al., 1982), in pink crystals with colourless rims. It  
188 can be either similar in size (size-compatible) or much smaller (size-incompatible) than the essential  
189 minerals, and more rarely much larger (size-incompatible) than the matrix minerals (granite from  
190 the Zemu glacier valley, VS10). Together with the other mineralogical components, the andalusite  
191 gives origin to a wide range of microstructures referred to the various textural classes of Clarke et  
192 al. (2005), summarised below.

### 193 3.2. *Andalusite textural types*

194 *Type S*: this is represented by euhedral to subhedral single grains in the matrix, and may also be  
195 found included in plagioclase cores. All types of microstructures, from those without muscovitic  
196 rims up to crystals almost completely replaced by large muscovite flakes, are observed (Fig 3g), in  
197 some cases in textural equilibrium with biotite (Fig. 3d). Subhedral to euhedral andalusite may be  
198 replaced by fibrolitic sillimanite or acicular (topotactic) sillimanite (Fig. 3l). Single subhedral to  
199 anhedral crystals lacking a muscovite mantle are found in the cores of zoned plagioclase (Fig. 3c).  
200 Relicts of corundum and prismatic sillimanite are found in the plagioclase of sample V731, together  
201 with anhedral andalusite.

202 *Type C*: is formed of two different types of clusters of randomly oriented grains, smaller than the  
203 magmatic minerals (size-incompatible). **a)** Optically discontinuous aggregates of subhedral to  
204 rounded crystals of variable size (0,05-0.25 mm), tightly packed and sometimes with brown

205 fibrolite borders (V928), interstitial or included in biotite, feldspar and quartz; remarkably, when  
 206 these clusters are hosted in biotite or plagioclase, the brown fibrolite border is missing (Fig. 3e, f  
 207 and m). **b)** Aggregates of euhedral crystals (0.15-0.3 mm), interstitial between the larger magmatic  
 208 crystals, and in places with a muscovite monocrystalline mantle (Fig. 3i). The two-mica  
 209 leucogranite from the Zemu glacier valley (VS10) is peculiar in that it consists of a medium-grained  
 210 (5 mm) granular rock with random quartz-K-feldspar graphic intergrowths containing skeletal  
 211 muscovite, suggesting rapid and cotectic crystallisation. Here andalusite is found in crystals up to  
 212 16 mm long, subparallel and grouped to form “veins” of poikilitic and in places skeletal grains. The  
 213 most common mineral inclusions in these poikilitic/skeletal crystals are laths of plagioclase, rounded  
 214 quartz and, more rarely, anhedral K-feldspar and subhedral biotite. Andalusite is typically replaced  
 215 by large monocrystalline muscovite, which may penetrate deeply along cracks, isolating rounded  
 216 fragments.

217

#### 218 4. Mineral chemistry

219 Mineral analyses were carried out with WDS CAMECA SX 50 electron microprobes  
 220 operating at 20 kV and 10 nA, with integration time of 10 s for major elements and 10 s for minor  
 221 elements; natural and synthetic pure oxides were used as standards for calibration. A PAP program  
 222 was used to convert counts into weight percents of oxides. Results are considered accurate to within  
 223  $\pm 2\%$  relative for major elements and  $\pm 5\%$  for minor elements.

224 Muscovite flakes growing on andalusite, single euhedral crystals in the matrix isolated from  
 225 biotite, and muscovite with euhedral contacts against biotite, were all analysed. Representative  
 226 analyses are listed in Tab. 1. Only a few of the muscovite grains have  $\text{TiO}_2$  concentrations  $> 1$  wt%,  
 227 suggesting a magmatic origin according to Miller et al. (1981). In undeformed granite, although the  
 228  $\text{Na}/(\text{Na}+\text{K})$  ratio is  $> 0.06$  (magmatic according to Monier et al., 1984, and Clarke et al., 2005),  
 229  $\text{TiO}_2$  contents of muscovite in single flakes far from biotite or growing on andalusite, were  
 230 commonly lower than those of muscovite in textural equilibrium with biotite. In the three samples  
 231 of foliated granite analysed (Tab. 2b), one two-mica granite (V953) and two tourmaline granites  
 232 (V218 and V927), the muscovite overgrowths on andalusite have  $\text{TiO}_2 < 0.05\%$  and  
 233  $\text{Na}/(\text{Na}+\text{K}) < 0.06$ .

234 Biotite crystals have high alumina contents over a very restricted interval ( $\text{Al}^{\text{IV}} = 2.68 \pm 0.07$ ,  
 235  $n=82$ ; Tab.1; Fig. 4a), suggesting that an Al-rich phase such as andalusite buffered the activity of  
 236  $\text{Al}_2\text{O}_3$  in the system during crystallisation. The composition of the texturally co-existing pairs of  
 237 muscovite-biotite are shown in Fig. 4b; the similar slope between all the tie-lines indicates that  
 238 these two minerals reached chemical equilibrium. The  $D_{\text{Ti}}^{\text{Bt-Ms}}$  ranges between 1.30-22.07;

239 excluding all values exceeding 8 (as recommended by Clarke et al., 2005), the mean value is  
240  $4.51 \pm 2.3$  (n=22). For micas with the above microstructures and compositions, this equilibrium was  
241 probably established in magmatic rather than subsolidus-hydrothermal conditions (Brigatti et al.,  
242 2000, Clarke et al., 2005).

243 Cordierite has only been found in two-mica granites. Euhedral crystals comparable in size  
244 with the quartzo-feldspathic matrix (but showing contrasting microstructures) were analyzed  
245 (analyzed crystals come from samples V23, Makalu; V472, Langma la; V93, Kharta). The  
246  $Fe/(Fe+Mg)$  ratio shows small variations (0.55-0.58) in samples V23 and V93, but a large variation  
247 in V472 (0.43-0.64; Tab 4). The cordierite in sample V23 shows well-defined chemical zoning,  
248 with the rim impoverished in MgO and Na<sub>2</sub>O. In general the high Na<sub>2</sub>O contents (up to 1.52 wt %)  
249 and abundance of channel cations (Ca, Na and K; Tab 4) found in all crystals are very similar to  
250 those of cordierite considered to crystallise from a felsic magma (e.g., Pereira and Bea, 1994 and  
251 references therein; Alasino et al., 2010).

252

## 253 **5. U-Pb zircon geochronology**

### 254 *5.1 Methods*

255 In-situ U-Pb geochronology was carried out by excimer laser ablation-ICPMS at the C.N.R.-  
256 IGG-U.O.S. of Pavia. Zircons were separated from granite sample V275 by conventional methods  
257 (crushing, heavy liquids, hand-picking). Zircons as free as possible from fractures and inclusions  
258 were mounted in epoxy resin, polished and characterised for internal structure by  
259 cathodoluminescence (CL). The laser ablation instrument couples an ArF excimer laser microprobe  
260 at 193 nm (Geolas200Q-Microlas) with a sector field high-resolution ICPMS Element I from  
261 Thermo Finnigan. The analytical method is described by Tiepolo (2003). Instrumental and laser-  
262 induced U/Pb fractionation values were corrected with the Plesovice zircon as external standard  
263 (Slama et al., 2008). The same integration intervals and spot sizes were used on both external  
264 standard and unknowns. The reference zircon 02123 (295 Ma; Ketchum et al., 2001) was analysed  
265 together with unknowns for quality control (Tab 4). Spot size was set at 20 microns and laser  
266 fluency at 12J/cm<sup>2</sup>. Data reduction was carried out with the Glitter software package (van  
267 Achterbergh et al., 2001) and reproducibility of standards was propagated to all determinations in  
268 quadrature. Concordia ages were determined and concordia plots were constructed with Isoplot/EX  
269 3.0 software (Ludwig, 2000). All errors are given at 2 $\sigma$  level.

### 270 *5.2 Results*

271 Zircon has prismatic habit and dimensions of 50 to 150 microns. CL images reveal a  
272 complex internal structure characterised by inner and external domains with different properties



273 (Fig. 5). The inner cores are bright and showed oscillatory or convolute zoning. The boundary  
274 between the inner and external domains is lobate and cuts the internal structures, indicating that  
275 partial resorption occurred. The inner cores are thus inherited zircons. The outer domains have low  
276 CL emissions and show relatively well-developed oscillatory zoning, typical of zircon growth in  
277 magmatic conditions.

278 Thirty-six U-Pb geochronologic determinations were carried out on both internal and  
279 external domains, and most of the results yielded concordant U-Pb ages. Seven analyses carried out  
280 on the external domains with low CL emission yielded concordant or slightly discordant Miocene  
281 ages (discordance 1.7% to 4.6%). The mean concordia age was  $15.9 \pm 0.4$  Ma (MSWD= 2.9; Fig.  
282 5). The ages of inherited cores ranged from 375 Ma to 1613 Ma, with major intermediate clusters at  
283 440 Ma and 780 Ma.

284

## 285 6. DISCUSSION

### 286 6.1 Origin of andalusite

#### 287 6.1.1 Major element composition of leucogranites.

288 The geochemical data of Visonà and Lombardo (2002) show that the leucogranites  
289 examined here (Tab. 6) have normative compositions near that of a low-pressure *minimum melt*  
290 ( $P=300-350$  MPa) in the wet haplogranite system. According to this and to the experimental data of  
291 Acosta-Vigil et al. (2003, 2006), the andalusite-bearing leucogranites are interpreted as low-  
292 pressure and relatively low-temperature melt rich in  $H_2O$ . For instance, the mean ASI value of 1.17  
293 matches the ASI of melts rich in  $H_2O$  in equilibrium with andalusite at the temperatures suggested  
294 by the normative compositions and Zrn and Mnz saturation thermometry (647-798 °C, Tab. 6). In  
295 addition, the occurrence of peritectic cordierite, only found in two-mica granites, indicates the  
296 involvement of biotite during melting, and this is consistent with the more mafic features of the  
297 two-mica granite (higher Mg, Ti, Fe, Sr, Y, Zr, Ba and REE) with respect to tourmaline granite  
298 (Holtz and Johannes, 1991; Icenhower and London, 1995, Acosta-Vigil et al., 2010). Petrographic  
299 evidence for the peritectic origin of the cordierite, according to the reaction  $sill+bt=cord+melt$ , was  
300 reported by Visonà and Lombardo (2002). The high content of  $Na_2O$  (up to 1.52 wt%, Tab. 4) and  
301 the abundance of channel cations (Ca, Na, K; Tab. 4) of euhedral cordierite also suggests its  
302 crystallisation in the presence of silicate melts (Pereira and Bea, 1994; Clarke, 1995; Alasino et al.,  
303 2010).

#### 304 6.1.2 Composition of biotite and muscovite

305 The microstructures are similar to those described in the literature for magmatic muscovite  
306 (Miller et al., 1981; Zen, 1988). In the unfoliated two-mica granite, the mineral chemistry of both

307 biotite and muscovite is compatible with their crystallisation from a magma ( $D_{Ti}^{Bt-Ms}$  mean  
 308  $4.51 \pm 2.3$ ). The high contents of alumina in the biotite of all samples ( $Al^{IV} = 2.68 \pm 0.07$ ) imply the  
 309 presence of an Al-rich phase (e.g. andalusite) saturating alumina in the magma already during the  
 310 crystallisation of biotite (Clarke et al., 2005). Therefore, the microstructures and composition of  
 311 micas indicate that andalusite is not a late-crystallising mineral but probably constitutes an early  
 312 phase in the magma.

313

314

### 315 *6.1.3 Microstructures of andalusite.*

316 The variety of microstructures in which andalusite is found, in cases within the same  
 317 sample, can be explained as due to different origins (e.g., metamorphic or magmatic) and/or to  
 318 crystallization from the magma at different stages (Clarke et al., 2005).

319 *Single-crystal grains (S).* This type of euhedral to subhedral andalusite, included in  
 320 plagioclase cores or size-compatible in the matrix, with or without a muscovite mantle, is probably  
 321 magmatic (i.e., magmatic-peritectic and/or magmatic-cotectic), and the crystals owe their shape to  
 322 the fact that they grew freely in the melt. Euhedral andalusite (lacking a muscovite mantle) in  
 323 plagioclase (Fig. 3a, b, g) may represent one of the first minerals present in a melt either saturated  
 324 in  $Al_2SiO_5$  from the source, or in which  $Al_2SiO_5$  saturation occurred (e.g.,  $ASI \geq 1.15$ ; Acosta-Vigil  
 325 et al, 2003; Clarke et al., 2005). It is also possible that these crystals represent peritectic andalusite  
 326 (crystallised during a peritectic reaction of the type  $mu + qtz + ab = and + melt$ ) as suggested by  
 327 inclusions of andalusite + quartz grains in plagioclase cores (Fig. 3b). With respect to the  
 328 andalusite-sillimanite stability field boundary proposed by Pattison (1992), the peritectic reaction  
 329  $mu + qtz + ab = Al_2SiO_5 + melt$  falls in the sillimanite field (Fig. 6). However, the andalusite-  
 330 sillimanite boundary after Richardson (1969) occurs at a higher temperature at constant pressure  
 331 (R69 in Fig. 6) and, in this case, the formation of peritectic andalusite would have been possible.  
 332 Either crystallised together with the melt (peritectic) or from the melt (cotectic), these  
 333 microstructures suggest that andalusite is not a late-crystallising phase, but was present early in the  
 334 history of the leucogranitic magma. Euhedral andalusite may also crystallise later, as a consequence  
 335 of late  $Al_2SiO_5$  saturation in the melt. This may be the case of the cm-sized peritectic andalusite  
 336 associated with dumortierite in the Zemu valley pegmatitic leucogranite, which perhaps resulted  
 337 from growth in a water-saturated melt (e.g., Whitney and Dilek, 2000; Clarke et al., 2005). Single  
 338 anhedral grains of andalusite in plagioclase (e.g., sample V731 in Fig 3c) may result from a reaction  
 339 between an andalusite of any origin (residual, peritectic or early magmatic) with the silicate melt  
 340 phase (Clarke et al., 2005). In particular, it is more probable that andalusite is residual in cases such

341 as that of sample V731, in which plagioclase also contains other residual minerals such as prismatic  
342 sillimanite and corundum. Microstructures of overgrowths of sillimanite after andalusite (residual or  
343 peritectic) like that shown in Fig. 3l suggest an increase in temperature after andalusite  
344 crystallisation. The overgrowth of a magmatic muscovite mantle (with  $\text{Na}/(\text{Na}+\text{K}) > 0.06$ ) on  
345 andalusite in the matrix is interpreted as a reaction during cooling between the residual magma and  
346 andalusite at low pressure (below 400 MPa), in the stability field of muscovite.

347 *Clustered grains (C)*. The existence of the size-incompatible (small) clustered andalusite  
348 grains leads to at least two different interpretations. In the interstitial clusters of euhedral to  
349 subhedral andalusite (sample V471, Fig. 3i) the crystals may have grown in the free spaces between  
350 the larger crystals which formed earlier, in which case the muscovite of their mantle would  
351 represent the last magmatic mineral to form. These microstructures are interpreted as result from  
352 late cotectic crystallization of andalusite in a magma saturated in  $\text{Al}_2\text{SiO}_5$ . Sample V471 also shows  
353 anhedral andalusite included in plagioclase, which may indicate that the magma was saturated or  
354 close to saturation in  $\text{Al}_2\text{SiO}_5$  during its early history, and probably throughout its history. The  
355 clusters of optically discontinuous rounded grains of different sizes included in biotite or  
356 plagioclase (e.g., sample V93, Fig. 2e) cannot be interpreted as quenched crystals formed during  
357 late crystallization of the magma. Instead, the inclusion of this type of cluster in early-crystallised  
358 silicates is consistent with a hypothesis of refractory residues. Experiments show that, at low  
359 pressure (e.g., 200-500 MPa), pelite is the most fertile rock, producing melts with andalusite  
360 residues (Thompson, 1996), the solubility of which in crustal melts is limited by the relatively low  
361 temperatures and, to lower extent, water contents (Acosta-Vigil et al., 2003). In conclusion, these  
362 clusters may represent concentrations of refractory residues in a partial melting scenario.

363 To summarise, the andalusite in single anhedral crystals included in plagioclase, those  
364 forming the clusters of packed crystals included totally or only partially in plagioclase and biotite,  
365 and those wrapped within sillimanite are all interpreted here as of probable residual origin. The  
366 single euhedral andalusite crystals included in plagioclase or interstitial probably have a peritectic  
367 or early cotectic origin. The interstitial clusters of euhedral to subhedral andalusite represent  
368 cotectic crystallisation in a magma saturated in  $\text{Al}_2\text{SiO}_5$ .

369

## 370 **6.2 Conditions of anatexis**

371 Most of the samples contain residual and/or magmatic (early and/or late) cotectic andalusite  
372 (e.g. sample V471), indicating that the whole P-T path from anatexis to melt solidification occurred  
373 at  $P \leq$  about 400 MPa (P92 triple point, Fig. 6). Considering the maximum pressure for andalusite  
374 stability and the location of the wet granite solidus, the minimum temperature indicated by the

375 formation of peritectic cordierite + melt, from sillimanite + biotite, is ~ 660-700 °C (Fig. 6).  
376 Temperatures up to 798 °C, obtained for the andalusite two-mica granite according to the  
377 concentrations of Zr and REE in the leucogranite (Tab. 6), probably represent an estimate of the  
378 maximum temperature of magma at its source (Miller et al., 2003). However, these T values may  
379 also be overestimated, due to the widespread occurrence of inherited zircon and monazite (e.g.  
380 Streule et al., 2010). At the temperatures suggested by Qtz-Or-Ab normative compositions and  
381 accessory thermometry, and in the presence of andalusite, the high ASI of the leucogranites  
382 suggests that the melt was relatively rich in water (Acosta-Vigil et al., 2002; 2003). Compared with  
383 the heating path, during cooling and crystallization of the magma, the pressure either remained  
384 constant or underwent a slight decrease, with a cooling path approximately parallel to that during  
385 prograde anatexis, as shown by the presence of andalusite throughout the history of the magma and  
386 by the formation of magmatic muscovite (Thompson and Algor, 1977; Clarke et al., 2005). The  
387 excess of alumina and the relatively high amounts of B and F in the melt (occurrence of tourmaline  
388 and fluorite, Visonà and Lombardo, 2002; replacements/overgrowths of cordierite by late  
389 tourmaline, this paper) probably decreased the temperature of the granite solidus with respect to that  
390 of H<sub>2</sub>O-saturated haplogranite melts (Manning, 1981; Pichavant, 1987; Holtz et al., 1992a, b;  
391 London, 1992). Consequently, the fields of magmatic andalusite and muscovite of the granite  
392 examined here extended towards lower P and T values. Fig. 6 shows the likely solidus of the  
393 andalusite leucogranite magmas during crystallisation (dashed curve in Fig. 6). Otherwise, later  
394 magmatic andalusite and muscovite, observed in the studied granites would not have formed.

395 The leucogranites examined here also commonly contains sillimanite, which may be either  
396 residual, magmatic (Visonà and Lombardo, 2002) or post-magmatic and subsolidus (Musumeci,  
397 2002; Kellett et al., 2009). The acicular sillimanite overgrowth on andalusite (Fig. 3l) is interpreted  
398 as a record of the prograde heating which caused dehydration melting of biotite in the sillimanite  
399 field (Fig. 6). In the foliated granites (e.g., sample 18d, Makalu), fibrous sillimanite is found in  
400 heterogeneous shear zones in which it is “disharmonious” (*sensu* Vernon and Flood, 1977) with  
401 respect to the muscovite in the foliation. In this case, as proposed for the neighbouring leucogranite  
402 of the Everest valley (Musumeci, 2002), the growth of sillimanite is subsolidus and results from the  
403 formation of heterogeneous shear zones. In unfoliated leucogranite (e.g., V472 and VS38), the  
404 brown fibrous sillimanite along the mineral junctions of the matrix (Fig 3a, e, f) is interpreted as the  
405 product of protonic hydrolysis (base-cation leaching; Vernon, 1987). According to this hypothesis,  
406 the agents responsible for leaching were not magmatic fluids, because they were already alkali-  
407 saturated, but probably metamorphic aqueous fluids. The unoriented acicular sillimanite replacing  
408 muscovite and biotite (e.g., sample V730, Fig. 3n) might represent the effects of a thermal event

409 which took place after the leucogranite solidification. However, in the absence of any other  
410 geological data supporting this interpretation, Kellett et al. (2009) suggested that, in the andalusite-  
411 bearing leucogranite of Bhutan, sillimanite grew in the andalusite field during magma cooling. In  
412 this context, the expansion of sillimanite stability towards lower temperatures requires the presence  
413 of magmatic fluids, and not metamorphic, with particular concentrations in transition metals  
414 (Grambling and Williams, 1985; Pattison, 1992), but no evidence of such fluids was found  
415 (andalusite contains negligible concentrations of transition elements; Tab. 5). Alternatively, this  
416 type of retrograde sillimanite may result from to a thermal event locally associated with  
417 heterogeneous shear zones, like that of the Everest valley leucogranite.

418

### 419 **6.3 Implications for the Himalaya orogeny**

420 The genesis of the andalusite leucogranites studied here is consistent with anatexis of  
421 metapelite during low-pressure prograde heating. This does not seem to match either original or  
422 currently proposed geodynamic models (e.g., extrusion and channel flow) that imply the generation  
423 of all the Himalayan leucogranite during decompression melting of the HHC (e.g., Harris et al.,  
424 1993; Patiño-Douce and Harris, 1998; Searle et al., 2010). The P-T evolution of the Himalayan  
425 metamorphism in the upper HHC (Barun gneiss, north of the High Himalayan Thrust – HHT in Fig  
426 1) of the Everest region and, further north, in the Mabjia dome (North Himalaya) is relatively well  
427 constrained, with an early prograde Barrovian event occurring at ~ 32-39 Ma and a later event at ~  
428 25-16 Ma (Lee and Whitehouse 2007; Jessup et al., 2008; Cottle et al., 2009b; M1 to M3 events of  
429 Pognante and Benna, 1993). During this time interval, with P diminishing from 600 to 400 MPa,  
430 there were two stages of migmatization and of magma production, at ~24 Ma and < 16 Ma,  
431 associated with the extrusion of the HHC (Simpson et al., 2000; Viskupic et al., 2005; Lee and  
432 Whitehouse 2007; Jessup et al., 2008; J. M. Cottle et al., 2009b; Streule et al., 2010). In this  
433 hypothesis of decompression melting of the HHC, andalusite may only form from the magma after  
434 its emplacement at the shallowest levels. The migmatitic stage which terminated at ~16 Ma is  
435 considered to represent the end of the south-directed channel flow (Murphy and Harrison, 1999;  
436 Cottle et al., 2009b; Streule et al., 2010). This second metamorphic event coincides in time and P-T  
437 conditions with the data derived from the andalusite leucogranites. Thus, the P-T estimates record a  
438 decrease in pressure to 300-200 MPa (Jessup et al., 2008; Streule et al., 2010), compatible with the  
439 growth of andalusite described in the structurally higher metapelitic levels of the HHC and in those  
440 at the base of the Everest Series (Palivcova et al., 1982; Pognante and Benna, 1993; Jessup et al.,  
441 2008). Also, in the Makalu pluton, two phases of granite emplacement have yielded ages of 24-21  
442 Ma (Schärer et al., 1986; Streule et al., 2010) and 15.7 Ma (Streule et al., 2010), which coincide

443 with the two main stages of migmatitisation recorded in the HHC rocks (see above). The studied  
444 andalusite leucogranite, which composes the higher part of this pluton (sampled at 7075 m), yields  
445 an age of  $15.9 \pm 0.4$  Ma, which is statistically equivalent to that reported by Streule et al. (2010) for  
446 the younger granitic pulse. These two ages also coincide with that of anatexis of  $16.0 \pm 0.6$  Ma  
447 (Streule et al., 2010) in the HHC immediately underlying the pluton, in which andalusite has been  
448 found in leucosomes (Pognante and Benna, 1993). The P and T conditions at the end of  
449 crystallisation in them and in the granite have values of about 200 MPa and 600 °C, and are viewed  
450 as constraining the clockwise P-T path from high-temperature to low-pressure metamorphism  
451 (Streule et al., 2010). These values, however, are not compatible with the formation of magmatic  
452 andalusite and muscovite in the leucogranite of the highest part of the Makalu pluton. Lastly, and in  
453 general, despite all the above coincidences in age and P-T conditions, there is one major problem,  
454 this andalusite leucogranite was probably generated at low pressure, and this is not compatible with  
455 the metamorphic evolution recorded in the HHC rocks (e.g. Groppo et al., 2012). Therefore, in the  
456 Everest-Makalu-Khartu area, the previously documented clockwise P-T path metamorphism in the  
457 extruding HHC could not have generated the andalusite leucogranite, because its formation requires  
458 low-pressure anatectic metamorphism of prograde character.

459 The occurrence of two types of leucogranites showing melting at intermediate pressure  
460 (originated by decompression; e.g., Searle et al., 2010, and references therein) and low pressure  
461 (formed by isobaric heating; this paper) may be explained in the following way. Because melting  
462 during heating at low pressure requires an extra input of heat (as documented by petrological data),  
463 this implies that hotter material (from below) came into contact with the source rocks of the  
464 andalusite leucogranites. The rocks above the andalusite-bearing leucogranite would be excluded,  
465 as they record a lower metamorphic grade with respect to the HHC rocks. One possibility is that  
466 normal faults/shear zones have put into contact colder rocks above and hotter rocks below.  
467 However, most authors agree that the general tectonic setting active during the exhumation and/or  
468 extrusion of the HHC was compressional. The contemporaneous activity of the upper STDS and  
469 lower MCT, bordering the HHC, drove the high- to medium-grade metamorphic rocks of the HHC  
470 to higher structural levels (Godin et al., 2006, and references therein). Taking into account two of  
471 the most popular models of exhumation of the HHC, such as extrusion and channel flow, we must  
472 consider that rocks are exhumed in a general flow derived from the combination of simple and pure  
473 shear components acting together (Law et al., 2004; Carosi et al., 2006, 2007). The  
474 contemporaneous activity of pure and simple shear components determines the parabolic shape of  
475 the velocity profiles of material particles moving across a vertical section through the HHC so that,  
476 schematically, particle velocities are higher in the middle of the tectonic unit and decrease towards

477 its boundaries (Godin et al., 2006; Grujic, 2006). A consequence is that hot rocks in the middle of  
478 the HHC moved faster than the rocks above (and below) them, so that, after some millions of years,  
479 hotter rocks from the middle part of the HHC may have come into contact with the colder rocks above  
480 (Fig. 7). In such a way, the hotter rocks may have generated an additional input of heat towards the  
481 relatively colder muscovite-bearing rocks above, causing them to melt during prograde heating at  
482 lower pressure and produce andalusite-bearing leucogranites. An increase of temperature at low  
483 pressure is compatible with the occurrence of late andalusite in the schists of the Everest valley  
484 (Jessup et al., 2008), in those of the high Barun valley (Palivcova et al., 1982; Pognante and  
485 Benna, 1993) and in the Ama Drime paragneissic unit (Kali et al., 2010). The interpretation that this  
486 andalusite represents a product of the metamorphic reaction at the end of the P-T clockwise  
487 decompression path is only acceptable for the Nupse-Lhotse pelite (Everest schists), which contain  
488 muscovite, but not for the other two cases (HHC pelite) in which mica must already have been  
489 consumed at higher temperatures during the decompressive anatectic phase. We therefore  
490 emphasise that, for the complete understanding of the orogenic evolution of the belt, several  
491 mechanisms for the generation of granite generation and, correspondingly, occurrence of two  
492 different P-T paths must be taken into account.

493 The occurrence of the younger andalusite-bearing leucogranite is compatible with the channel  
494 flow or general extrusion models proposed for the HHC, but it is not enough to discriminate  
495 between the two models (Carosi et al., 2006, 2010). In any case, the available structural and  
496 kinematic data (Carosi et al., 2006, 2010) currently reveal no evidence of extensional faults or shear  
497 zones, and support the hypothesis of exhumation in a general compressive tectonic setting.

498

## 499 7. Conclusions

500 Andalusite-bearing leucogranites outcrop in a well-defined area in the central-eastern sector  
501 of the Himalayan belt. The residual and/or magmatic peritectic origin of andalusite in most of the  
502 studied leucogranites constrains anatexis at low pressure conditions during prograde heating. The  
503 age of 16 Ma obtained from the upper portion of the Makalu leucogranite links the generation of  
504 andalusite-bearing leucogranites with the most recent anatectic-metamorphic event documented in  
505 the area.

506 Dehydration melting of muscovite during heating and/or decompression of the HHC, often  
507 invoked as a suitable mechanism for the generation of the Himalayan leucogranites, took place in  
508 the sillimanite field and thus cannot explain the production of leucogranites at low pressure ( $P <$   
509 about 400 MPa). P and T conditions for anatexis in the andalusite field could only have taken place  
510 at higher structural levels, and with the input of some extra heat. This input of heat may have been

511 caused by the exhumation of the HHC by non-coaxial deformation (e.g., simple shear + pure shear).  
 512 In this model, the path of particles during exhumation was parabolic in shape, and the more  
 513 exhumed (and hotter) portion occurred in the middle portion of the HHC (Fig. 7). The more  
 514 exhumed central and hotter parts of the HHC may have come into contact with the upper and  
 515 colder parts, made of fertile lithologies. In this way, if during exhumation the velocity of  
 516 displacement parallel to the tectonic boundaries did not overcome the velocity of heat conduction  
 517 (nearly perpendicular to tectonic boundaries), the higher part of the HHC would have received  
 518 enough heat to produce (new) anatexis and the formation of subsolidus sillimanite in the already  
 519 generated granite.

520 In conclusion, a simple decompression model is not appropriate to explain the occurrence of  
 521 andalusite-bearing leucogranites. Two events of anatexis, in the sillimanite and andalusite stability  
 522 fields, respectively, are necessary to explain the generation of all the leucogranites outcropping in  
 523 the HHC and north Himalayan domes.

524

## 525 **Acknowledgements**

526 This research was funded by the Universities of Padova (V.D.) and Pisa (R.C., C.M.), PRIN  
 527 Cofin 2006. We wish to thank A. Acosta-Vigil and D. B. Clarke, who greatly improved the  
 528 manuscript with their constructive criticism and helpful suggestions, P. Pertusati for lively  
 529 discussions in the field and for sharing his knowledge of metamorphic structures and rocks. Mineral  
 530 analyses were acquired in the electron microprobe laboratories of the Department of Earth Sciences,  
 531 University of Padova. We would also like to thank the guide Diego Fregona for collecting samples  
 532 and geological pictures along the "French path" during the Italian Makalu expedition in 2002  
 533 (Barun base camp – Maklalu La-Summit Makalu). The English version of the Italian text was  
 534 translated by Gabriel Walton.

535

536

## 537 **REFERENCES**

- 538 van Achterbergh, E., Ryan, C.G., Jackson, S.E., Griffin, W., 2001. Data reduction software for LA-  
 539 ICP-MS. In: Sylvester, P. (ed.) Laser Ablation-ICPMS in the Earth Sciences. Mineralogical  
 540 Association of Canada, Short Course Series 29, 239-243.
- 541 Acosta-Vigil, A., Pereira, M.D., Shaw, D.M., London, D., 2001. Contrasting behavior of B during  
 542 crustal anatexis. *Lithos* 56, 15-31.
- 543 Acosta-Vigil, A., London, D., Dewers, T.A., Morgan VI, G.B., 2002. Dissolution of corundum and  
 544 andalusite in H<sub>2</sub>O-saturated haplogranitic melts at 800 °C and 200 MPa: constraints on  
 545 diffusivities and the generation of peraluminous melts. *Journal of Petrology* 43, 1885-1908.
- 546 Acosta-Vigil, A., London, D., Morgan VI, G.B., Dewers, T.A., 2003. Solubility of excess alumina  
 547 in hydrous granitic melts in equilibrium with peraluminous minerals at 700-800 °C and 200



- 548 MPa, and applications of the aluminum saturation index. *Contributions to Mineralogy and*  
 549 *Petrology* 146, 100-119.
- 550 Acosta-Vigil, A., London, D., Morgan VI, G.B., 2006. Experiments on the kinetics of partial  
 551 melting of a leucogranite at 200MPa and 690-800 °C: compositional variability of melts  
 552 during the onset of H<sub>2</sub>O-saturated crustal anatexis. *Contributions to Mineralogy and Petrology*  
 553 151, 539-557.
- 554 Acosta-Vigil A., Buick, I., Hermann, J., Cesare, B., Rubatto, D., London, D., Morgan VI, G.B.,  
 555 2010. Mechanisms of crustal anatexis; a geochemical study of partial melted metapelitic  
 556 enclaves and host dacite, SE Spain. *Journal of Petrology* 51, 785-821.
- 557 Alasino, P.H., Dahlquist, J.A., Galindo, C., Casquet, C., Saavedra, J., 2010. Andalusite and Na- and  
 558 Li-rich cordierite in the La Costa pluton, Sierra Pampeanas, Argentina: textural and chemical  
 559 evidence for a magmatic origin. *International Journal of Earth Science* 99, 1051-1065.
- 560 Beaumont, C., Jamieson, R.A., Nguyen, M.H., Lee, B., 2001. Himalayan tectonics explained by  
 561 extrusion of a low-viscosity crustal channel coupled to focused surface denudation, *Nature*  
 562 414, 738–742, doi:10.1038/414738a.
- 563 Bordet, P., 1961. *Recherches géologiques dans l'Himalaya du Nepal, région du Makalu*. Editions du  
 564 Centre National de la Recherche Scientifique, Paris, 275 pp.
- 565 Borghi, A., Castelli, D., Lombardo, B., Visona', D., 2003. Thermal and baric evolution of garnet  
 566 granulites from the Kharta region of S Tibet, E Himalaya. *European Journal of Mineralogy*  
 567 15(2), 401-418.
- 568 Brigatti, M.F., Frigieri, P., Ghezzi, C., Poppi, L., 2000. Crystal chemistry of Al-rich biotites  
 569 coexisting with muscovites in peraluminous granites. *American Mineralogist* 85, 436–448.
- 570 Burchfiel, B.C., Chen, Z., Hodges, K.V., Liu, Y., Royden, L.H., Deng, C., Xu, J., 1992. The South  
 571 Tibetan Detachment System, Himalayan Orogen: extension contemporaneous with and  
 572 parallel to shortening in a collisional mountain belt. *The Geological Society of America*  
 573 *Special Paper* 269, 41 pp.
- 574 Carosi, R., Montomoli, C., Rubatto, D., Visona', D., 2006. Normal-sense shear zones in the core of  
 575 the Higher Himalayan Crystallines (Bhutan Himalayas): evidence for exstrusion? In: Law,  
 576 R.D., Searle, M., Godin, L. (Eds.), *Channel Flow, Ductile Extrusion and Exhumation of*  
 577 *Lower-mid Crust in Continental Collision Zones*. Geological Society of London, Special  
 578 Publication 268, 425-444.
- 579 Carosi, R., Montomoli, C., Visona', D., 2007. A structural transect in the Lower Dolpo: Insights on  
 580 the tectonic evolution of Western Nepal. *Journal of Asian Earth Sciences*, 29, 407-423.
- 581 Carosi, R., Montomoli, C., Rubatto, D., Visona', D., 2010. Late Oligocene high-temperature shear  
 582 zones in the core of the Higher Himalayan Crystallines (Lower Dolpo, Western Nepal).  
 583 *Tectonics*, 29: TC4029, doi:10.1029/2008TC002400.
- 584 Castelli, D., Lombardo, B., 1988. The Gophu La and Western Lunana granites: Miocene muscovite  
 585 leucogranites of the Bhutan Himalaya. *Lithos* 21, 211 – 225.
- 586 Clarke, D.B., 1995. Cordierite in felsic igneous rocks: a synthesis. *Mineralogical Magazine* 59, 311  
 587 – 325.
- 588 Clarke, D.B., Dorais, M., Barbarin, B., Barker, D., Cesare, B., Clarke, G., el Baghdadi, M.,  
 589 Erdmann, S., Förster, H-J., Gaeta, M., Gottesmann, B., Jamieson, R.A., Kontak, D.J., Koller,  
 590 F., Gomes, C.L., London, D., Morgan VI, G.B., Neves, L.J.P.F., Pattison, D.R.M., Pereira,  
 591 A.J.S.C., Pichavant, M., Rapela, C., Renno, A.D., Richards, S., Roberts, M., Rottura, A.,  
 592 Saavedra, J., Sial, A.N., Toselli, A.J., Ugidos, J.M., Uher, P., Villaseca, C., Visonà, D.,  
 593 Whitney, D.L., Williamson, B., Woodard, H.H., 2005. Occurrence and origin of andalusite in  
 594 peraluminous felsic igneous rocks. *Journal of Petrology* 46, 441–472. doi:  
 595 10.1093/petrology/egh083.
- 596 Clarke, D.B., 2007. Assimilation of xenocrysts in granitic magmas: Principles, processes, proxies,  
 597 and problems. *The Canadian Mineralogist* Vol. 45, 5-30.

- 598 Clarke, D.B., Wunder, B., Förster, H.J., Rhede, D., Hahn, A., 2009. Experimental investigation of  
599 near-liquidus andalusite-topaz relations in synthetic peraluminous haplogranites at 200 MPa.  
600 *Mineralogical Magazine* 73(6), 997–1007.
- 601 Cottle, J.M., Jessup, M.J.; Newell, D.L., Horstwood, M.S.A., Noble, S.R.; Parrish, R.R., Waters, D.  
602 J., Searle, M.P., 2009a. Geochronology of granulitized eclogites from the Ama Drime Massif,  
603 implications for the tectonic evolution of the South Tibetan Himalaya. *Tectonics* 28:TC1002.
- 604 Cottle, J.M., Searle, M.P., Horstwood, M.S.A., Waters, D., 2009b. Timing of midcrustal  
605 metamorphism, melting, and deformation in the Mount Everest region of southern Tibet  
606 revealed by U(-Th)-Pb geochronology. *Journal of Geology* 117, 643–664.
- 607 Debon, F., Le Fort, P., 1983. A chemical– mineralogical classification of common plutonic rocks  
608 and associations: principles, methods, applications. *Bulletin de Mineralogie* 111, 493– 510.
- 609 Debon, F., Le Fort, P., Sheppard, S.M., Sonet, J., 1986. The four plutonic belts of the  
610 Transhimalaya-Himalaya: a chemical, mineralogical, isotopic, and chronological synthesis  
611 along a Tibet-Nepal section. *Journal of Petrology* 27(1), 219-250.
- 612 Dèzes, P., 1999. Tectonic and metamorphic evolution of the Central Himalayan domain in  
613 Southeast Zaskar (Kashmir, India). *Mémoires de Géologie (Lausanne)* 32, 145pp.
- 614 Gansser, A., 1964. *Geology of the Himalayas*. Wiley-Interscience, London.
- 615 Godin, L., Grujic, D., Law, R.D., Searle, M.P., 2006. Channel flow, ductile extrusion and  
616 exhumation in continental collision zones: An introduction, in: Law, R.D., Searle, M.P.,  
617 Godin, L. (Eds.), *Channel Flow, Ductile Extrusion and Exhumation in Continental Collision*  
618 *Zones*. Geological Society, London, Special Publication 268, 1–23.
- 619 Grambling, J.A., Williams, M.L., 1985. The effects of Fe<sup>3+</sup> and Mn<sup>3+</sup> on aluminum silicate phase  
620 relations in north-central New Mexico, U.S.A.: *Journal of Petrology* 26(2), 324-354.
- 621 Groppo, C., Rolfo, F., Indares, A., 2012. Partial melting in the Higher Himalayan Crystallines of  
622 Eastern Nepal: the effect of decompression and implications for the ‘Channel Flow’ model.  
623 *Journal of Petrology*, 1-32, doi:10.1093/petrology/egs009.
- 624 Grujic, D., 2006. Channel flow and continental collision tectonics; an overview, in: Law, R.D.,  
625 Searle, M.P., Godin, L. (Eds.), *Channel Flow, Ductile Extrusion and Exhumation in*  
626 *Continental Collision Zones*. Geological Society, London, Special Publication, 268, 25-37.
- 627 Guillot, S., Le Fort, P., 1995. Geochemical constraints on the bimodal origin of High Himalayan  
628 leucogranites. *Lithos* 35, 221–234.
- 629 Harris, N., Inger, S. and Massey, J. (1993). The role of fluids in the of High Himalayan  
630 leucogranites. In: Searle, M., P., Treloar, P., J., (eds) *Himalayan Tectonics*. *Geological*  
631 *Society, London, Special Publication* 74, 391–400.
- 632 Holtz, F., Johannes, W., 1991. Genesis of peraluminous granites: I. Experimental investigation of  
633 melt compositions at 3 and 5 kb and various H<sub>2</sub>O activities. *Journal of Petrology* 32, 935–  
634 958.
- 635 Holtz F, Johannes W, Pichavant M (1992a) Peraluminous granites: the effect of alumina on melt  
636 composition and coexisting minerals. *Transactions of the Royal Society of Edinburgh: Earth*  
637 *and Environmental Science*, 83:409–416
- 638 Holtz F, Johannes W, Pichavant M (1992b) Effect of excess aluminum on phase relations in the  
639 system Qz-Ab-Or. Experimental investigation at 2 kbar and reduced H<sub>2</sub>O activity. *European*  
640 *Journal of Mineralogy*, 4, 137–152
- 641 Jessup, M.J., Cottle, J.M., Searle, M.P., Law, R.D., Newell, D.L., Tracy, R.J., Waters, D.J., 2008.  
642 P-T-t-D paths of Everest Series schists, Nepal. *Journal of Metamorphic Geology* 26, 717-  
643 739.
- 644 Kali, E., Leloup, P.H., Arnaud, N., Mahéo, G., Liu, D., Boutonnet, E., Vanderwoerd, J., Liu X., Jing  
645 Liu - Zeng, Haibing Li, 2010. Exhumation history of the deepest central Himalayan rocks, Ama  
646 Drime range: Key pressure-temperature-deformation-time constraints on orogenic models  
647 *Tectonics*, 29; TC2014, doi:10.1029/2009TC002551.

- 648 Kellett, D.A., Grujic, D., Erdmann, S., 2009. Miocene structural reorganization of the South Tibetan  
649 detachment, eastern Himalaya: Implications for continental collision. *Lithosphere*, 1(5), 259-  
650 281.
- 651 Ketchum, J.W.F., Jackson, S.E., Culshaw, N.G., Barr, S.M., 2001. Depositional and tectonic setting  
652 of the Paleoproterozoic Lower Aillik Group, Makkovik Province, Canada: evolution of a  
653 passive margin-foredeep sequence based on petrochemistry and UPb (TIMS and LAM-ICP-  
654 MS) geochronology. *Precambrian Research* 105, 331-356.
- 655 Kretz, R., 1983. Symbols for rock-forming minerals. *American Mineralogist* 68, 277–279.
- 656 Icenhower, J.P., London, D., 1995. An experimental study of element partitioning among biotite,  
657 muscovite, and coexisting peraluminous silicic melt at 200 MPa (H<sub>2</sub>O). *American*  
658 *Mineralogist* 80, 1229–1251.
- 659 Larson, K.P., Godin, L., Davis, W.J., Davis, D.W., 2010. Out-of-sequence deformation and  
660 expansion of the Himalayan orogenic wedge: insight from the Changgo culmination, south  
661 central Tibet. *Tectonics*, 29: TC4013, doi:10.1029/2008TC002393.
- 662 Law, R.D., Searle, M.P., Simpson, R.L., 2004. Strain, deformation temperatures and vorticity of  
663 flow at the top of the Greater Himalayan Slab, Everest Massif, Tibet. *Journal of the*  
664 *Geological Society* 161, 305–320.
- 665 Le Fort, P., 1975. Himalayas: the collided range. Present knowledge of the continental arc.  
666 *American Journal of Science*, 275-a: 1-44.
- 667 Lee, J., Hacker, B., Wang, Y., 2004. Evolution of North Himalayan gneiss domes: structural and  
668 metamorphic studies in Mabja Dome, southern Tibet. *Journal of Structural Geology*, 26(12),  
669 2297-2316.
- 670 Lee, J., McClelland, W., Wang, Y., Blythe, A., McWilliams, M.O., 2006. Oligocene-Miocene  
671 middle crustal flow in southern Tibet: geochronology of Mabja Dome. In: Law, R. D., Searle,  
672 M. P., Godin, L. (Eds.), *Channel Flow, Ductile Extrusion and Exhumation in Continental*  
673 *Collision Zones*. Geological Society, London, Special Publications 74, 445-469.
- 674 Lee, J., Whitehouse, M. J., 2007. Onset of mid-crustal extensional flow in southern Tibet: Evidence  
675 from U/Pb zircon ages. *Geology* 35,45-48.
- 676 London, D., 1992. The application of experimental petrology to the genesis and crystallization of  
677 granitic pegmatites. *Canada Mineralogist*, 30, 499-540.
- 678 Ludwig, K.R., 2000. *Isoplot a geochronological toolkit for Microsoft Excel*. Berkeley  
679 Geochronology Center, Special Publications 1a, 53 p.
- 680 Manning, D., A., C., 1981. The effect of fluorine on liquidus phase relationships in the system Qz-  
681 Ab-Or with excess water at 1 kb. *Contribution to Mineralogy and Petrology*, 76, 206-215.
- 682 Miller, C.F., Stoddard, E.F., Bradfish, L.J., Dollase, W.A., 1981. Composition of plutonic  
683 muscovite: genetic implications. *The Canadian Mineralogist* 19, 25-34.
- 684 Miller, C.F., McDowell, S.M., Mapes, R.W., 2003. Hot and cold granites? Implications of zircon  
685 saturation temperatures and preservation on inheritance. *Geology* 31, 529-532.
- 686 Monier, G., Mergoïl-Daniel, J., Labernardiere, H., 1984. Generations successives de muscovites et  
687 feldspaths potassiques dans les leucogranite du massif de Millevaches (Massif Central  
688 français). *Bulletin de Mineralogie* 107, 55–68.
- 689 Mosca, P., Groppo, C. Rolfo, F., 2010. Structural and metamorphic architecture of the Himalayas in  
690 the Kangchenjunga area (far-Eastern Nepal). *Rendiconti on line*, II, 423-424.
- 691 Murphy, M., Harrison, T.M., 1999. Relationship between leucogranites and the Qomolangma  
692 detachment in the Rongbuk Valley, south Tibet. *Geology* 27, 831– 834.
- 693 Musumeci, G., 2002. Sillimanite-bearing shear zones in syntectonic leucogranite: fluid- assisted  
694 brittle-ductile deformation under amphibolites facies conditions. *Journal of Structural*  
695 *Geology* 24, 1491-1505.
- 696 Palivcova, M., Kalvoda, J., Minarik, L., 1982. Petrology of the Makalu massif, Nepal Himalayas.  
697 *Rozpr. Cesk. Akad.Ved* 92 (2), 1 – 69.

- 698 Patiño-Douce, A., Harris, N., 1998. Experimental constraints on Himalayan anatexis. *Journal of*  
699 *Petrology*, 39, 689– 710.
- 700 Pattison, D.R.M., 1992. Stability of andalusite and sillimanite and the Al<sub>2</sub>SiO<sub>5</sub> triple point:  
701 constraints from the Ballachulish aureole, Scotland. *Journal of Geology* 100, 423– 446.
- 702 Pereira , M.D., Bea, F., 1994. Cordierite-producing reactions in the Peña Negra Complex, Avila  
703 batholith, Central Spain: the key role of cordierite in low-pressure anatexis. *The Canadian*  
704 *Mineralogist*, 32, 763-780.
- 705 Pichavant, M., 1987. Effect of B and H<sub>2</sub>O on liquidus phase relations in the haplogranitic system at  
706 1 kbar. *American Mineralogist*, 72, 1056-1070.
- 707 Pognante, U., Benna P., 1993. Metamorphic zonation, migmatization, and leucogranites along the  
708 Everest transect of Eastern Nepal and Tibet: record of an exhumation history. *in: Treloar, P.J.,*  
709 *Searle, M.P., (Eds ), Himalayan Tectonics, Geological Society of London Special*  
710 *Publication, 74, 323- 340.*
- 711 Richardson, S.W., Gilbert, M.C., Bell, P.M., (1969). Experimental determination of kyanite –  
712 andalusite and andalusite–sillimanite equilibria; the aluminum silicate triple point. *American*  
713 *Journal of Science* 267, 259–272.
- 714 Rolfo, F., Carosi, R., Montomoli, C., Visonà, D., Villa, I. M., 2006. A geological transect east of  
715 Kangchendzonga (North Sikkim, India). *Journal of Asian Earth Sciences*, 26: 158.
- 716 Schärer, U., Xu, R. H., and Allegre, C.J., 1984. U-Pb geochronology of Gandese (Transhimalaya)  
717 plutonism in the Lhasa-Xigaze region, Tibet. *Earth and Planetary Science Letters*, 69, 311-  
718 320.
- 719 Schärer, U., Xu, R-H, and Allègre, C.J., 1986. U-(Th)-Pb systematics and ages of Himalayan  
720 leucogranites, South Tibet. *Earth and Planetary Science Letters*, 77, 35-48.
- 721 Searle, M.P., Cottle, J.M., Streule, M.J., Waters, D.J., 2010. *Earth and Environmental Science*  
722 *Transactions of the Royal Society of Edinburgh* 100, 219-233.
- 723 Simpson, R.L., Parrish, R.R., Searle, M.P, Waters, D.J., 2000. Two episodes of monazite  
724 crystallization during metamorphism and crustal melting in the Everest region of the  
725 Nepalese Himalaya. *Geology* 28, 403-406.
- 726 Sláma, J., Košler, J., Condon, D.J., Crowley, J.L., Gerdes, A., Hanchar, J. M., Horstwood, M.S.A.,  
727 Morris, G.A., Nasdala, L., Norberg, N., Schaltegger, U., Schöne, B., Tubrett, M. N.,  
728 Whitehouse, M.J., 2008. Plešovice zircon — A new natural reference material for U–Pb and  
729 Hf isotopic microanalysis. *Chemical Geology* 249, 1-35.
- 730 Streule. M.J., Searle, M.P., Waters, D.J., Matthew, S.A., Horstwood, M.S.A., 2010. Metamorphism,  
731 melting and channel flow in the Greater Himalaya Sequence and Makalu leucogranite:  
732 constraints from thermobarometry, metamorphic modelling and U-Pb geochronology.  
733 *Tectonics* 29: TC5011, doi:10.1029/2009TC002533.
- 734 Thompson, A.B., Algor, J.R., 1977. Model systems for anatexis of pelitic rocks *Contributions to*  
735 *Mineralogy and Petrology* 63, 247-269.
- 736 Thompson, A.B., 1996. Fertility of crustal rocks during anatexis. *Transactions of Royal Society of*  
737 *Edinburgh: Earth Sciences* 87, 1-10, 1996.
- 738 Tiepolo, M., 2003. In situ Pb geochronology of zircon with laser ablation-inductively coupled  
739 plasma-sector field mass spectrometry. *Chemical Geology* 199 159-177.
- 740 Vernon, R.H., and Flood, R.H., 1977. Interpretation of metamorphic assemblages containing  
741 fibrolitic sillimanite. *Contributions to Mineralogy and Petrology.* 59, 277-235.
- 742 Vernon, R.H., 1987. Formation of late sillimanite by hydrogen metasomatism (base leaching) in  
743 some high grade gneisses. *Lithos* 79, 143-152.
- 744 Viskupic, K., Hodges, K.V., Bowring, S.A., 2005. Timescales of melt generation and the thermal  
745 evolution of the Himalayan metamorphic core, Everest region, eastern Nepal, *Contributions to*  
746 *Mineralogy and Petrology* 149(1), 1–21.

- 747 Visonà, D., Lombardo, B., 2002. Two mica- and tourmaline leucogranites from the Everest-Makalu  
748 region (Nepal-Tibet). *Himalayan leucogranite genesis by isobaric heating?* *Lithos* 62(3-4):  
749 125-150.
- 750 White, R.W., Powell, R., Holland, T.J.B., 2001. Calculation of partial melting equilibria in the  
751 system Na<sub>2</sub>O–CaO–K<sub>2</sub>O–FeO–MgO–Al<sub>2</sub>O<sub>3</sub>–SiO<sub>2</sub>–H<sub>2</sub>O (NCKFMASH). *Journal of*  
752 *Metamorphic Geology* 19 (2), 139–53.
- 753 Whitney, D.L., Dilek, Y., 2000. Andalusite–sillimanite–quartz veins as indicators of low-pressure–  
754 high-temperature deformation during late-stage unroofing of a metamorphic core complex,  
755 Turkey. *Journal of Metamorphic Geology* 18, 59–66.
- 756 Zhang, H., Harris, N., Parrish, R.R., Kelley, S., Zhang, L., Rogers, N., Argles, T., King, J., 2004.  
757 Causes and consequences of protracted melting of the mid-crust exposed in the North  
758 Himalayan antiform. *Earth and Planetary Science Letters* 228(1-2): 195-212.
- 759 Zen, E-an, 1986. Aluminium enrichment in silicate melt by fractional crystallization: some  
760 mineralogic and petrographic constraints. *Journal of Petrology* 27, 1095-1117.
- 761 Zen, E-an, 1988. Phase relations of peraluminous granitic rocks and their petrogenetic implications.  
762 *Annual Review of Earth and Planetary Sciences* 16, 21–51.

## 763 CAPTIONS

- 764
- 765
- 766 **CAPTIONS**
- 767
- 768 **Fig 1.** Simplified geological map of central (-east) Himalayan range from Gansser (1983),  
769 Burchfiel et al. (1992), with modifications by Grujic et al. (2002) and Cottle et al (2007).  
770 High Himalayan Thrust (HHT) divides upper from lower structural level of HHC. Stars:  
771 locations of Miocene leucogranite with andalusite known in literature: 1, Debon et al. (1986);  
772 2 and 3, Zhang et al. (2004); 4, Palivcova et al. (1982), Pognante and Benna (1993); 5, Mosca  
773 et al. (2010); 6, Rolfo et al. (2006); 7, Kellett et al. (2009); 8, Castelli and Lombardo (1988).  
774
- 775 **Fig 2.** Location of study samples on radar map. Black numbers: andalusite leucogranite with  
776 subsolidus sillimanite. UHHC: upper HHC; LHHC: Lower HHC; HHT: High Himalayan  
777 Thrust; STDS: South Tibetan Detachment System. Tectonic boundaries from Kali et al.  
778 (2010).  
779
- 780 **Fig 3.** Photomicrographs illustrating andalusite and sillimanite textures, symbols of minerals as  
781 Kretz (1983). a – sample VS38a: brown fibrolitic sillimanite around a plagioclase enclosing a  
782 single andalusite grain without sillimanite border; b – sample VS38b: a grain of  
783 andalusite+quartz in a plagioclase core; c – sample V731: single anhedral pink andalusite  
784 enclosed in plagioclase; d – sample V328: single andalusite grain replaced by euhedral  
785 muscovite in euhedral contact with biotite; e, f – sample V93: clusters of small, randomly  
786 oriented andalusite grains enclosed in biotite and (f) a single euhedral andalusite, brown  
787 fibrolitic sillimanite fills mineral junction in matrix; g – sample V328b: single andalusite  
788 grain with muscovite mantle in matrix, but without muscovite mantle when enclosed in  
789 plagioclase; h (b)- sample V927: single andalusite grain with subsolidus muscovite mantle  
790 (Na/(Na+K) = 0.052); i – sample V471: intergranular cluster of randomly oriented subhedral  
791 andalusite with muscovite mantle; l – V473: subhedral andalusite replaced by acicular  
792 sillimanite; m – sample V472: intergranular cluster of randomly oriented, packed, rounded



793 andalusite partially enclosed in plagioclase; brown sillimanite grows on clusters only outside  
794 plagioclase; n - sample V730: acicular sillimanite growing on biotite.

795

796 **Fig 4.** Compositions of coexisting micas. **(a)** Biotite compositions in phlogopite-annite-eastonite-  
797 siderophyllite system. **(b)** Molecular (FeO+MnO+MgO) vs. TiO<sub>2</sub>. Tie lines join coexisting  
798 muscovite and biotite pairs.

799

800 **Fig 5.** A) Cathodoluminescence images of representative zircon grains, with location of laser  
801 ablation spot. B) Concordant ages obtained on zircon domains with low CL emission and  
802 mean concordia age. All errors given at 2 sigma level.

803

804 **Fig 6.** P-T diagram showing paths during generation and crystallisation of studied leucogranite, as  
805 constrained by andalusite and magmatic muscovite stability. Comparison with P-T path  
806 proposed for Miocene metamorphism in upper HHC of Makalu area (Pognante and  
807 Benna, 1993; Streule et al., 2010). 1) metapelite melting, curves for metamorphic and melting  
808 reactions in muscovite- and biotite-metapelite from White et al. (2001); 2) hypothetical  
809 position of H<sub>2</sub>O-saturated Al-saturated boron-rich granite solidus. Al<sub>2</sub>SiO<sub>5</sub> phase relations  
810 after Pattison (1992) (P92) and Richardson et al. (1969) (R69). Symbols of minerals as Kretz  
811 (1983). Grey area: low pressure stability field of magmatic muscovite.

812

813 **Fig. 7.** Sketch (not to scale) of hypothesised interpretative model for generation of andalusite-  
814 bearing leucogranite. Higher Himalayan Crystallines tectonic unit is confined between the  
815 upper STDS (South Tibetan Detachment System) and the lower MCT (Main Central Thrust).  
816 Light grey arrows: represent parabolic particle velocity path in the HHC. Boxes: are rocks  
817 located at different structural levels in the tectonic units. Dark grey boxes: are deeper rocks  
818 which that move faster upwards towards the surface and at low pressure can transfer heat to  
819 upper colder rocks above (light grey box, upper left), giving rise to andalusite-bearing  
820 leucogranite. Deeper rocks in the core of HHC (dark grey box, lower right) may have  
821 originated leucogranite, owing to decompression melting.

822

823 **TAB 1.** Representative compositions of biotite and muscovite in textural equilibrium.  $D_{Ti}^{Bt-Ms}$   
824 range is 1.30-22.07, excluding all values greater than 8.00; mean  $4.51 \pm 2.3$  (n=22): attainment  
825 of chemical equilibrium between mica pairs.

826

827 **TAB 2.** Representative compositions of muscovite: A) magmatic; B) in deformed granite. TiO<sub>2</sub> and  
828 Na/(Na+K) ratio values are typical of non-igneous mica (Monier et al., 1984).

829

830 **TAB 3.** Cordierite analysis of three samples. Sample V23 is zoned and has high Na<sub>2</sub>O content,  
831 comparable to that of magmatic cordierite.

832

833 **TAB 4.** Representative compositions of andalusite; contents of transition elements is very low in all  
834 grains analysed.

835

836 **TAB 5.** U/Pb isotope ratios of zircon and apparent ages.

837

838 **TAB 6.** Major element compositions and accessory thermometry of two-mica andalusite  
 839 leucogranite from Everest-Masang Kang area. Data sources: a) Makalu: Palivcova et al.  
 840 (1982); b) Lagoi Kangri dome: Debon et al., 1986; c) Gophu Ka and Lunana: Castelli and  
 841 Lombardo (1988); d) Makalu-Kharta area: Visonà and Lombardo (2002); e) Mabja-Kuday  
 842 dome: Zhang et al. (2004); f) this work.

843

844

845

846

847

848

849

850

851

852

853

854 **APPENDIX**

855 **Sampled areas.** *Makalu.* Palivcova et al. (1982) described the Makalu West Wall as formed of two  
 856 overlapping units, both consisting of schists and granite and separated by a low-angle, north-  
 857 dipping thrust. The lower unit mainly contains cataclastic tourmaline granite with cordierite and  
 858 sillimanite. The upper unit consists of a lower thin injection zone (about 1000 m thick) with schists  
 859 and highly leucocratic granite (containing tourmaline, cordierite, garnet and sillimanite), and an  
 860 upper zone (at least 2000 m thick) essentially composed of fine-grained two-mica granite,  
 861 containing centimetric pods of tourmaline and occasionally sillimanite and andalusite. The upper  
 862 unit was sampled in 2002 by an Italian mountaineering expedition above the “injection zone” along  
 863 the path towards Makalu La and the main peak. Between altitudes of 6600 to 7450 m, two-mica  
 864 granites with sporadic centimetric pods of tourmaline and rare tourmaline granite occur. Samples  
 865 with andalusite were collected at altitudes of 6650, 7075 and 7400 m (V2-3, V275 and V218,  
 866 respectively. Fig 2) and, in the latter case, the two-mica granite, was in contact with a small body of  
 867 tourmaline granite, also containing andalusite.

868 *In the Kama Chu-Phung Chu (Kharta)-Rongbuk area, the sampled dykes cut the garnet-  
 869 sillimanite Kharta gneiss (Borghi et al., 2003) slightly above the hanging wall of the western side of  
 870 the Ama Drime Massif (sample locations: Fig. 2). Dykes of andalusite-bearing leucogranite (two-  
 871 mica granite, V953 and foliated tourmaline granite, V927) also occur within the Ama Drime  
 872 orthogneiss unit (Kali et al., 2010). Sample V916 was collected from debris of andalusite-bearing  
 873 tourmaline granite from higher parts of the Ama Drime range. Dykes of two-mica andalusite-  
 874 bearing leucogranite were found in the HHC immediately below the South Tibetan Detachment*

875 near Doya La (VDL), and a foliated and deformed dyke of tourmaline granite (V391) was sampled  
876 along the road in the Rongbuk valley.

877 Kangchenjunga-Sikkim area. In the Zemu valley (about 4500 m), a two-mica granite was  
878 sampled (with andalusite, cordierite and brown fibrolite, sample VS14), together with a peculiar  
879 two-mica leucogranite containing pink andalusite veinlets, up to 5 mm thick, parallel to the foliation  
880 in the rock (sample VS10). Sample VS38 comes from pseudo-concordant sills of two-mica granite  
881 (with cordierite, brown fibrolite and xenocrystic sillimanite) cutting the uppermost part of the HHC  
882 north of Yume Sandong.

883



Figure 1

[Click here to download high resolution image](#)

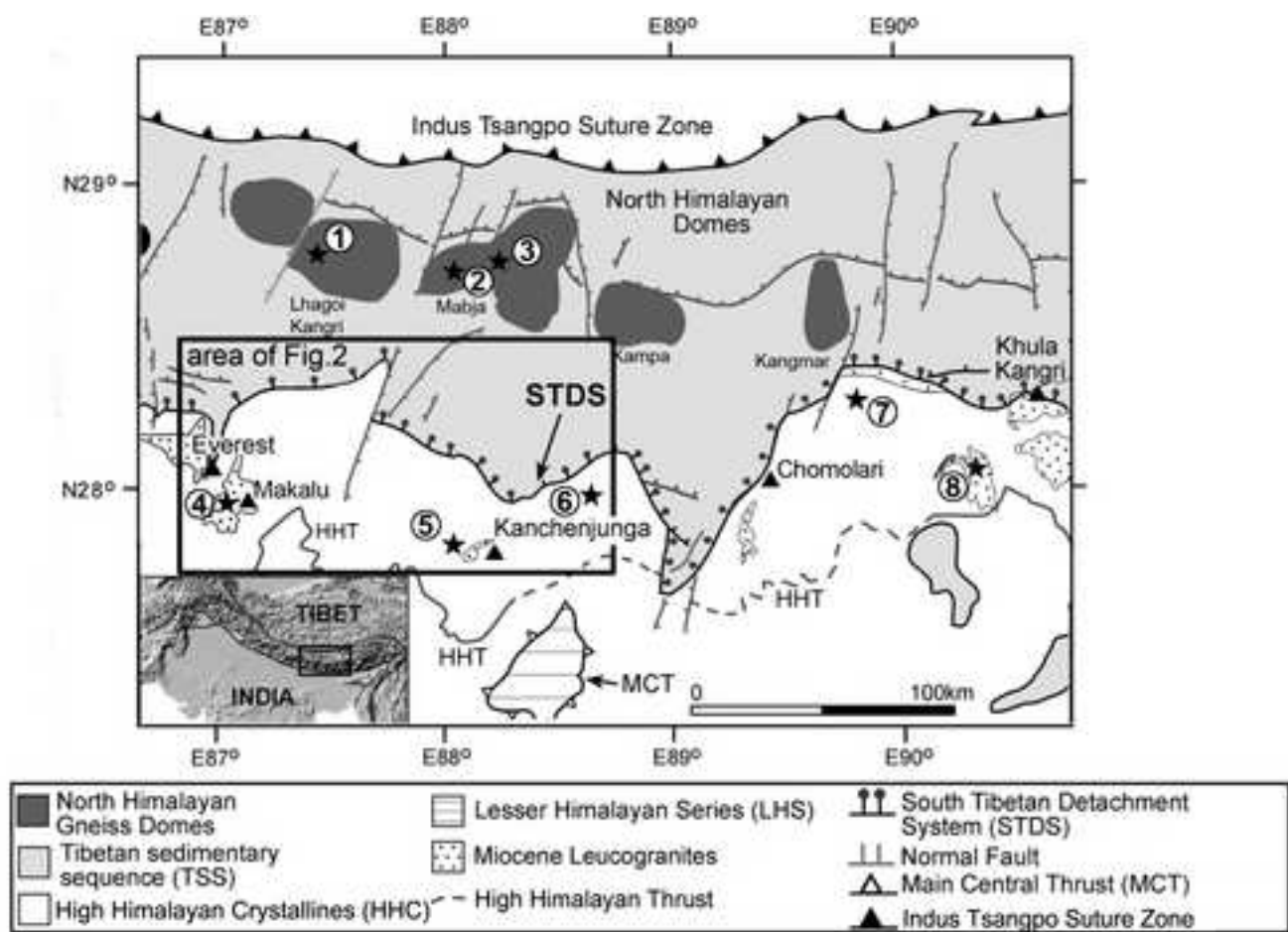


Figure 2

[Click here to download high resolution image](#)

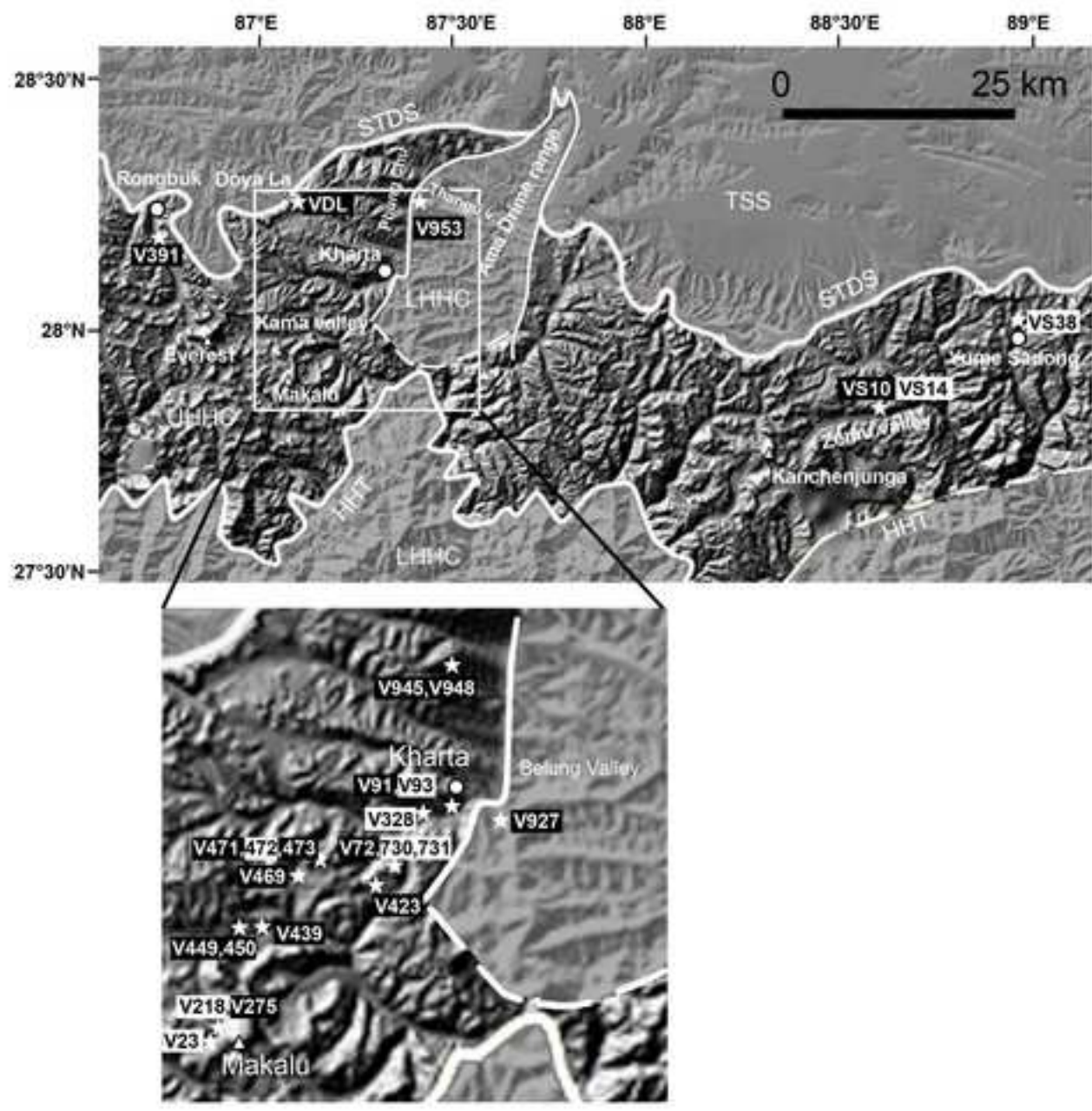




Figure 3  
[Click here to download high resolution image](#)

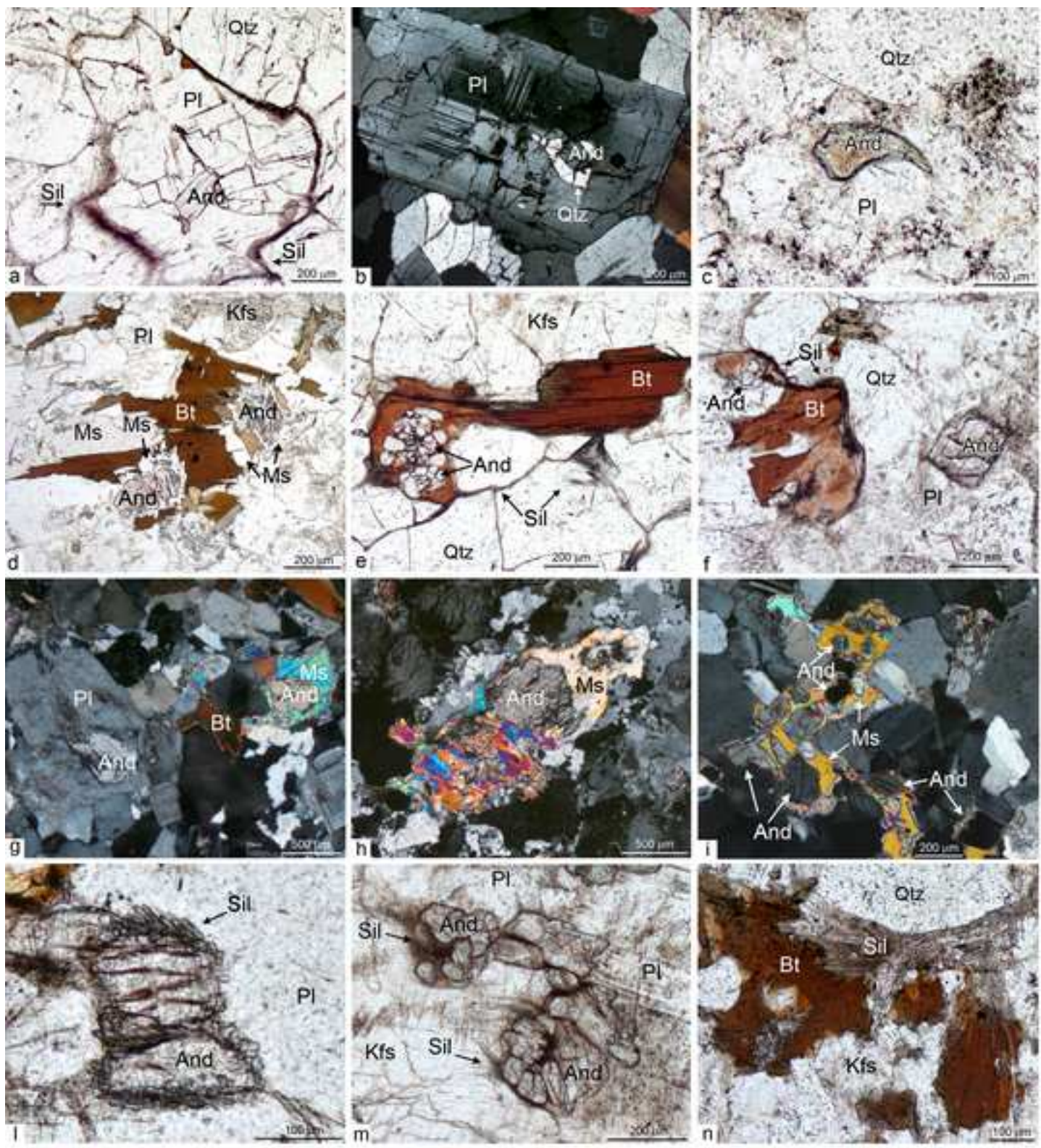


Figure 4

[Click here to download high resolution image](#)

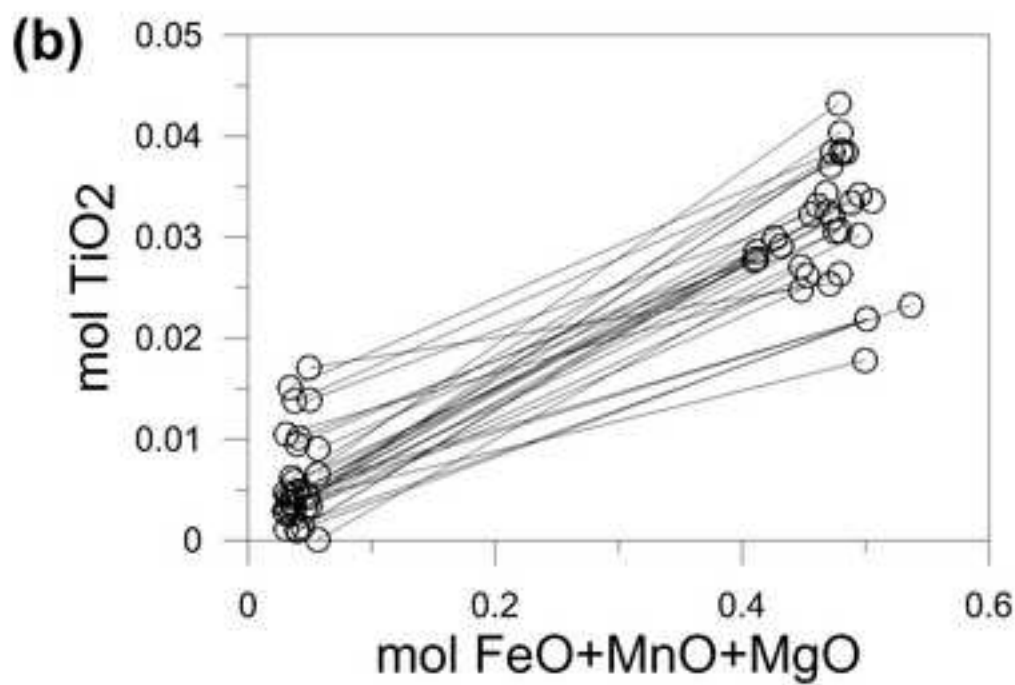
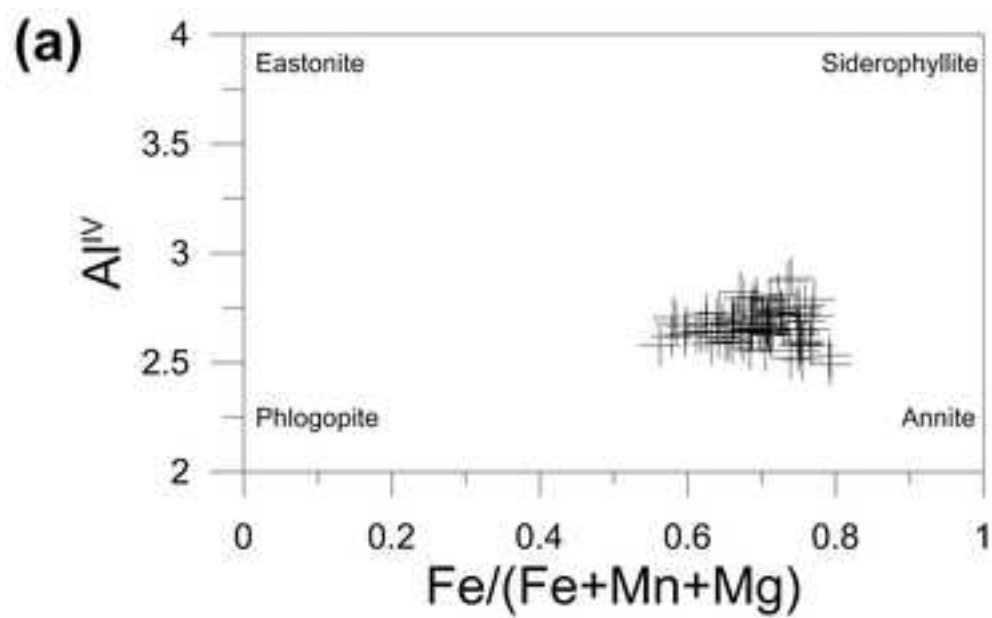
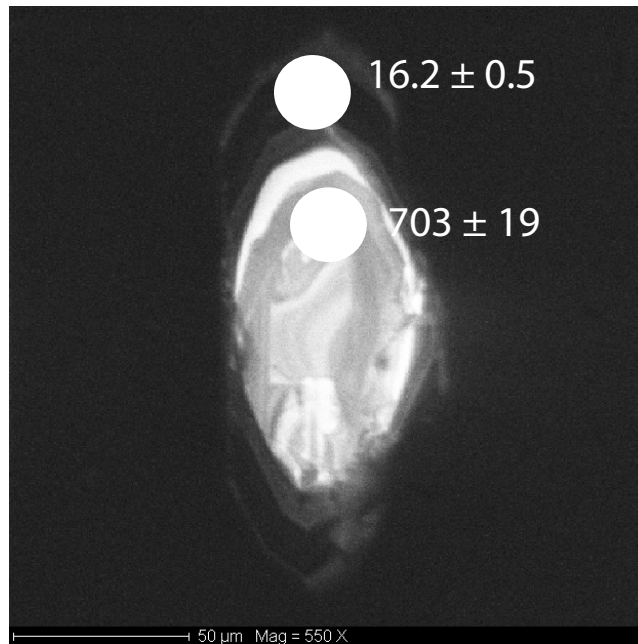
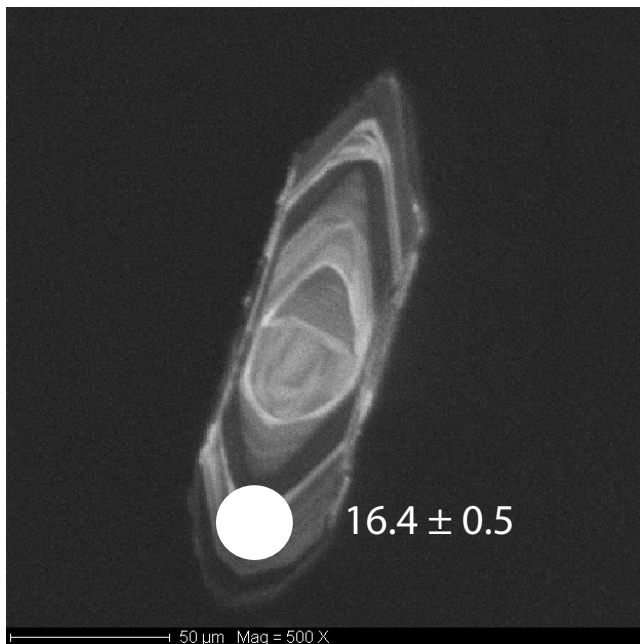


Fig 4



Figure 5



Concordia Age =  $15.9 \pm 0.4$  Ma  
(95% confidence, decay-const. errs included)  
MSWD (of concordance) = 2.9,  
Probability (of concordance) = 0.088

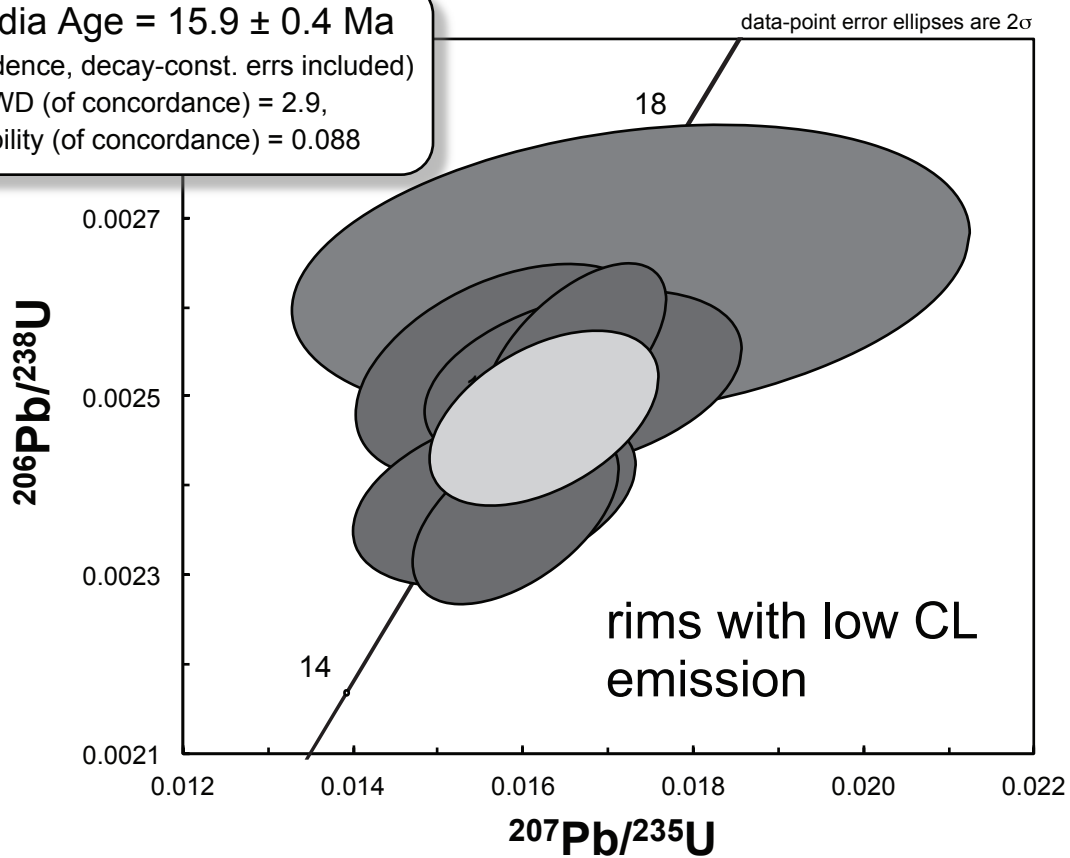


Figure 6  
[Click here to download high resolution image](#)

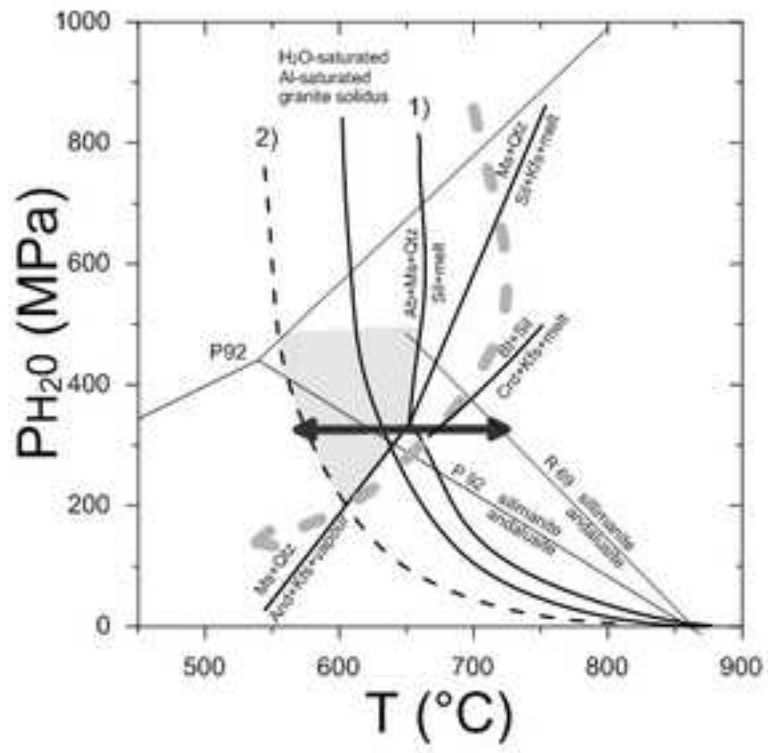


Figure 7  
[Click here to download high resolution image](#)

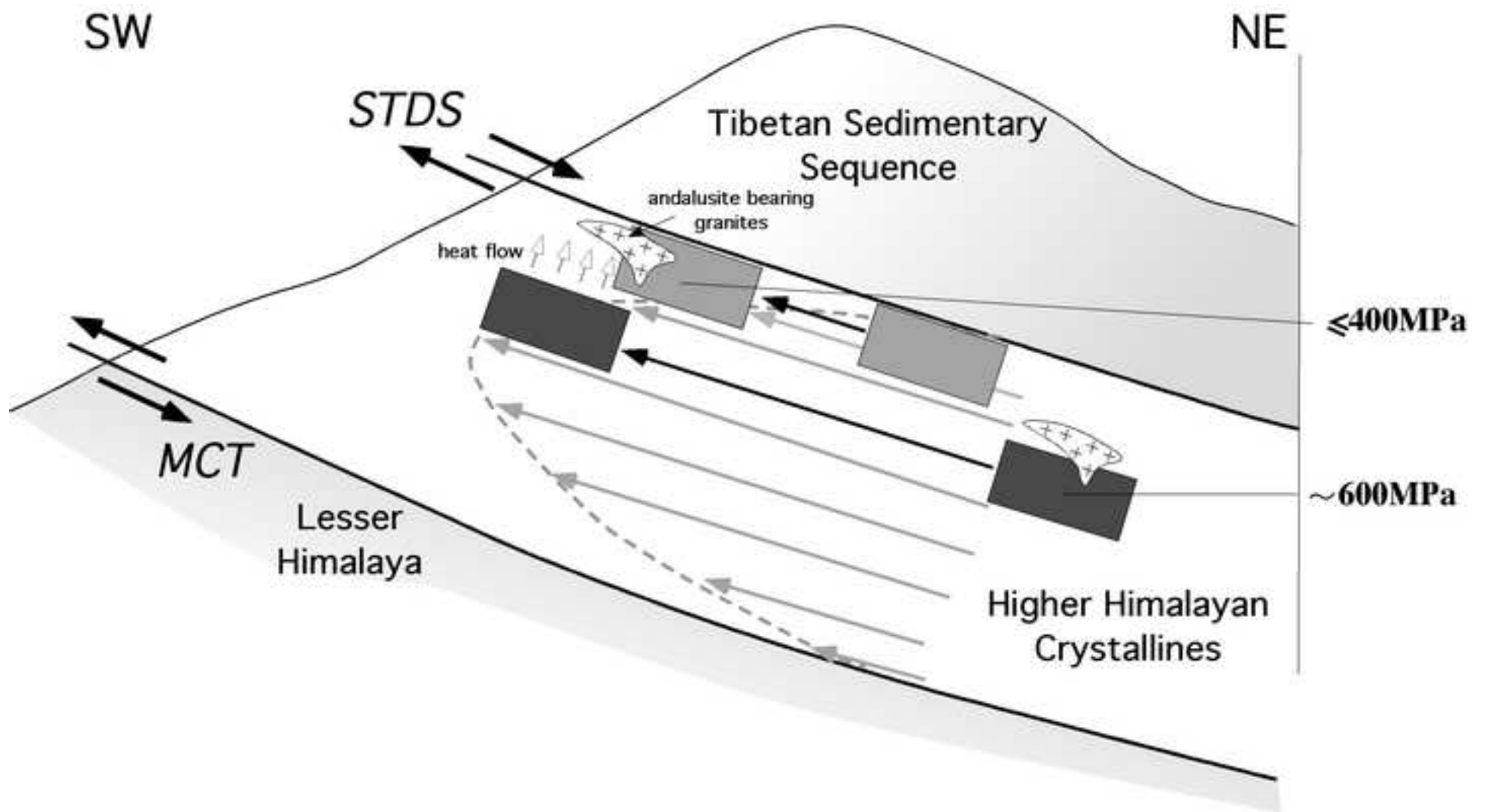


Table 1

[Click here to download Table: Table 1.xlsx](#)

Tab 1

	V328		VS38		V449		V945		VS10		V275		V439		V23		V730	
	mu	bt	mu	bt	mu	bt	mu	bt	mu	bt	mu	bt	mu	bt	mu	bt	mu	bt
SiO <sub>2</sub>	45.76	35.40	46.37	35.76	45.91	34.79	45.86	34.89	46.45	35.52	45.88	35.98	46.04	34.63	45.91	34.76	45.50	30.62
TiO <sub>2</sub>	0.22	1.17	1.32	3.17	0.50	2.91	0.27	1.98	0.84	2.11	0.81	2.23	1.21	3.07	1.11	2.58	0.23	1.86
Al <sub>2</sub> O <sub>3</sub>	34.18	20.35	34.58	19.55	34.99	19.87	34.68	20.57	35.90	19.81	34.93	20.51	35.17	19.49	34.55	19.59	36.10	21.01
Cr <sub>2</sub> O <sub>3</sub>	0.04	0.00	0.00	0.01	0.04	0.04	0.00	0.00	0.00	0.02	0.00	0.05	0.00	0.03	0.00	0.00	0.00	0.01
FeO	2.40	21.85	1.19	22.86	1.58	22.86	2.05	24.61	1.26	22.44	1.51	23.46	1.24	24.82	1.76	22.93	1.38	29.21
MnO	0.07	0.56	0.00	0.25	0.05	0.50	0.09	0.57	0.00	0.36	0.00	0.69	0.00	0.39	0.09	0.23	0.00	0.62
MgO	0.92	7.25	0.71	6.03	0.91	4.92	0.81	3.91	0.54	6.52	0.80	3.04	0.67	4.94	0.98	5.37	0.41	4.90
CaO	0.00	0.02	0.00	0.01	0.01	0.00	0.02	0.00	0.03	0.00	0.00	0.01	0.00	0.00	0.02	0.00	0.00	0.05
Na <sub>2</sub> O	0.42	0.13	0.54	0.12	0.70	0.00	0.58	0.01	0.68	0.14	0.69	0.00	0.54	0.00	0.59	0.00	0.70	0.03
K <sub>2</sub> O	10.58	9.51	10.38	9.36	10.17	9.12	9.86	8.93	10.17	9.05	9.82	9.01	10.49	9.23	10.30	9.36	10.35	5.82
F	0.46	0.76	0.21	1.06	0.56	0.60	0.63	1.18	0.26	0.48	1.11	1.09	0.11	0.45	0.79	1.98	0.12	0.00
Total	95.04	96.98	95.30	98.19	95.42	95.60	94.84	96.66	96.13	96.44	95.57	96.07	95.46	97.03	96.10	96.82	94.79	94.12
O=F,Cl	-0.19	-0.32	-0.09	-0.45	-0.24	-0.25	-0.26	-0.50	-0.11	-0.20	-0.47	-0.46	-0.05	-0.19	-0.33	-0.83	-0.05	0.00
Total	94.85	96.66	95.21	97.75	95.18	95.35	94.58	96.16	96.02	96.24	95.10	95.61	95.42	96.84	95.77	95.98	94.74	94.12
Numbers of ions on the basis of 23 O																		
Si	6.153	5.353	6.168	5.354	6.112	5.361	6.141	5.345	6.116	5.400	6.085	5.503	6.120	5.313	6.085	5.291	6.088	4.908
Al <sup>IV</sup>	1.847	2.647	1.832	2.646	1.888	2.639	1.859	2.655	1.884	2.600	1.915	2.497	1.880	2.687	1.915	2.709	1.912	3.092
Al <sup>VI</sup>	3.569	0.979	3.589	0.802	3.602	0.969	3.614	1.060	3.688	0.949	3.544	1.200	3.631	0.836	3.482	0.806	3.782	0.877
Ti	0.022	0.133	0.132	0.357	0.050	0.337	0.027	0.228	0.084	0.241	0.081	0.256	0.121	0.354	0.111	0.295	0.023	0.225
Cr	0.004	0.000	0.000	0.001	0.004	0.005	0.000	0.000	0.000	0.003	0.000	0.006	0.000	0.003	0.000	0.000	0.000	0.002
Fe <sup>2+</sup>	0.270	2.763	0.132	2.862	0.176	2.947	0.230	3.154	0.138	2.854	0.168	3.000	0.138	3.184	0.195	2.919	0.155	3.916
Mn	0.008	0.072	0.000	0.032	0.006	0.065	0.011	0.074	0.000	0.046	0.000	0.089	0.000	0.051	0.010	0.030	0.000	0.084
Mg	0.184	1.634	0.141	1.346	0.180	1.129	0.161	0.894	0.107	1.477	0.159	0.694	0.133	1.130	0.193	1.219	0.081	1.171
Sito O	4.057	5.580	3.994	5.400	4.018	5.453	4.043	5.409	4.017	5.569	3.952	5.246	4.022	5.559	3.991	5.269	4.041	6.274
Ca	0.000	0.003	0.000	0.002	0.002	0.000	0.002	0.000	0.004	0.000	0.001	0.001	0.000	0.000	0.002	0.003	0.000	0.009
Na	0.119	0.038	0.139	0.034	0.180	0.000	0.151	0.003	0.173	0.040	0.178	0.000	0.139	0.000	0.150	0.000	0.183	0.008
K	1.814	1.835	1.762	1.788	1.727	1.792	1.685	1.746	1.708	1.755	1.662	1.757	1.779	1.806	1.742	1.818	1.767	1.190
Sito A	1.922	1.876	1.901	1.824	1.908	1.792	1.839	1.749	1.885	1.795	1.841	1.758	1.917	1.806	1.894	1.821	1.950	1.207
F	0.194	0.363	0.090	0.504	0.236	0.291	0.265	0.573	0.107	0.232	0.464	0.527	0.046	0.217	0.331	0.951	0.051	0.000
Total	14.17	15.82	13.98	15.73	14.16	15.54	14.15	15.73	14.01	15.60	14.26	15.53	13.99	15.58	14.22	16.04	14.04	15.48
O=F,Cl	-0.19	-0.36	-0.09	-0.50	-0.24	-0.29	-0.26	-0.57	-0.11	-0.23	-0.46	-0.53	-0.05	-0.22	-0.33	-0.95	-0.05	0.00
Total	13.98	15.46	13.90	15.22	13.93	15.25	13.88	15.16	13.90	15.36	13.79	15.00	13.94	15.36	13.89	15.09	13.99	15.48
AlTot	5.416	3.626	5.421	3.448	5.490	3.608	5.473	3.714	5.572	3.549	5.459	3.697	5.511	3.524	5.397	3.515	5.693	3.969
Na/(Na+K)	0.061	0.020	0.073	0.018	0.094	0.000	0.082	0.002	0.092	0.022	0.097	0.000	0.072	0.000	0.080	0.000	0.094	0.007
$D_{Ti}^{Bt/Ms}$	5.355		2.408		1.309		7.413		2.498		2.745		2.537		2.320		7.995	



Tab 2

	A) magmatic muscovite replacing andalusite										B) muscovite in deformed granites								
	VS10				VM3		V439		V730		replacing andalusite						with sillimanite		
	SK10E1	SK10E1	SK10E1	10B12	3-1A4	3-1A5	39a8	39a9	30B2	30B4	V953	V927	V927	V927	V927	V927	V218	V218	V218
SiO <sub>2</sub>	46.39	45.68	46.95	46.32	46.78	48.57	46.38	46.30	46.35	46.08	45.78	46.77	46.34	45.66	44.17	44.95	42.38	42.22	42.88
TiO <sub>2</sub>	0.05	0.00	0.30	0.00	0.34	0.00	0.03	0.24	0.06	0.07	0.03	0.05	0.03	0.03	0.00	0.06	0.01	0.02	0.00
Al <sub>2</sub> O <sub>3</sub>	37.81	38.77	36.08	36.95	35.50	33.74	36.45	35.76	36.68	36.36	36.27	37.13	36.34	37.16	37.10	36.21	33.29	27.28	31.54
Cr <sub>2</sub> O <sub>3</sub>	0.00	0.00	0.00	0.00	0.00	0.01	0.04	0.00	0.00	0.01	0.01	0.03	0.01	0.00	0.01	0.05	0.00	0.04	0.00
FeO	0.33	0.26	1.05	0.82	1.77	1.19	1.36	1.46	1.12	1.51	1.18	0.85	1.17	1.43	0.79	1.29	4.58	9.02	5.76
MnO	0.03	0.00	0.04	0.00	0.00	0.03	0.01	0.00	0.03	0.01	0.00	0.00	0.04	0.00	0.05	0.04	0.02	0.10	0.15
MgO	0.04	0.00	0.55	0.30	0.96	0.52	0.46	0.69	0.34	0.34	0.53	0.60	0.70	0.15	0.06	0.13	2.49	6.88	4.29
CaO	0.00	0.00	0.00	0.03	0.00	0.00	0.00	0.02	0.00	0.00	0.01	0.01	0.00	0.02	0.00	0.00	0.03	0.01	0.00
Na <sub>2</sub> O	0.78	0.73	0.81	0.53	0.75	0.47	0.76	0.56	0.71	0.59	0.43	0.42	0.39	0.37	0.40	0.36	0.36	0.22	0.25
K <sub>2</sub> O	9.94	10.13	9.93	10.29	10.11	10.12	10.16	10.17	10.53	10.09	10.83	10.75	10.69	10.45	10.58	10.33	10.16	10.05	10.48
F	0.14	0.00	0.60	0.50	0.68	0.04	0.37	0.27	0.35	0.11	0.42	0.00	0.38	0.00	0.00	0.36	0.00	0.14	0.39
Total	95.51	95.57	96.31	95.73	96.89	94.68	96.04	95.47	96.16	95.15	95.51	96.61	96.08	95.27	93.14	93.78	93.33	95.99	95.75
O=F,Cl	-0.06	0.00	-0.25	-0.21	-0.29	-0.02	-0.16	-0.11	-0.15	-0.04	-0.18	0.00	-0.16	0.00	0.00	-0.15	0.00	-0.06	-0.17
Total	95.45	95.57	96.06	95.52	96.61	94.66	95.88	95.35	96.02	95.11	95.33	96.61	95.92	95.26	93.14	93.63	93.33	95.93	95.58
Numbers of ions on the basis of 23 O																			
Si	6.098	6.008	6.150	6.102	6.126	6.454	6.112	6.140	6.104	6.125	6.084	6.119	6.111	6.069	6.004	6.071	5.899	5.897	5.881
Al <sup>IV</sup>	1.902	1.992	1.850	1.898	1.874	1.546	1.888	1.860	1.896	1.875	1.916	1.881	1.889	1.931	1.996	1.929	2.101	2.103	2.119
Al <sup>VI</sup>	3.955	4.016	3.721	3.840	3.606	3.738	3.773	3.729	3.797	3.821	3.766	3.843	3.759	3.889	3.947	3.836	3.361	2.388	2.979
Ti	0.005	0.000	0.030	0.000	0.034	0.000	0.003	0.024	0.006	0.007	0.003	0.005	0.003	0.003	0.000	0.006	0.001	0.002	0.000
Cr	0.000	0.000	0.000	0.000	0.000	0.001	0.004	0.000	0.000	0.001	0.001	0.003	0.001	0.000	0.001	0.005	0.000	0.005	0.000
Fe <sup>2+</sup>	0.036	0.029	0.115	0.090	0.193	0.132	0.150	0.162	0.123	0.167	0.131	0.093	0.129	0.159	0.090	0.146	0.533	1.054	0.660
Mn	0.003	0.000	0.004	0.000	0.000	0.003	0.001	0.000	0.003	0.001	0.000	0.000	0.004	0.000	0.005	0.005	0.003	0.012	0.018
Mg	0.009	0.000	0.107	0.060	0.187	0.103	0.090	0.136	0.067	0.067	0.105	0.117	0.138	0.029	0.012	0.027	0.516	1.433	0.877
Sito O	4.008	4.045	3.977	3.990	4.020	3.977	4.021	4.051	3.996	4.065	4.007	4.060	4.034	4.081	4.054	4.024	4.413	4.895	4.534
Ca	0.000	0.000	0.000	0.004	0.000	0.000	0.001	0.003	0.000	0.000	0.002	0.002	0.000	0.003	0.000	0.000	0.004	0.001	0.000
Na	0.199	0.185	0.206	0.134	0.190	0.121	0.195	0.145	0.182	0.152	0.111	0.108	0.099	0.095	0.105	0.095	0.098	0.060	0.068
K	1.668	1.700	1.660	1.730	1.690	1.715	1.708	1.720	1.769	1.711	1.837	1.794	1.798	1.773	1.834	1.779	1.804	1.791	1.833
Sito A	1.866	1.885	1.866	1.868	1.879	1.837	1.904	1.868	1.951	1.863	1.950	1.904	1.897	1.870	1.940	1.874	1.907	1.852	1.901
F	0.056	0.000	0.250	0.207	0.281	0.017	0.156	0.113	0.145	0.045	0.175	0.000	0.157	0.000	0.000	0.153	0.000	0.063	0.170
Total	13.930	13.931	14.092	14.065	14.180	13.830	14.082	14.031	14.092	13.973	14.13	13.96	14.09	13.95	13.99	13.90	14.32	14.75	14.44
O=F,Cl	-0.056	0.000	-0.250	-0.207	-0.281	-0.017	-0.156	-0.113	-0.145	-0.045	-0.18	0.00	-0.16	0.00	0.00	-0.15	0.00	-0.06	-0.17
Total	13.874	13.931	13.842	13.858	13.899	13.813	13.926	13.918	13.947	13.928	13.96	13.96	13.93	13.95	13.99	14.05	14.32	14.81	14.61
AlTot	5.857	6.009	5.570	5.738	5.479	5.284	5.661	5.589	5.693	5.696	5.682	5.724	5.648	5.821	5.944	5.765	5.462	4.492	5.098
Na/(Na+K)	0.106	0.098	0.110	0.072	0.101	0.066	0.103	0.078	0.093	0.082	0.057	0.057	0.052	0.051	0.054	0.051	0.052	0.032	0.036

**Tab 3**

	V93		V275	V328*	V423		V439*		V927*	V948*	V449	V953	VS10*			VS38		VM3*		
	core	rim			core	rim	core*	rim					core*	int*	rim*	core	core	core*	core*	rim*
SiO2	36.49	36.41	36.90	36.47	35.96	36.74	36.93	36.89	36.51	36.53	36.47	36.39	36.88	36.60	36.69	37.34	37.07	36.77	37.13	36.69
TiO2	0.03	0.03	0.01	0.02	0.02	0.11	0.06	0.08	0.03	0.06	0.05	0.05	0.11	0.06	0.08	0.04	0.06	0.09	0.01	0.01
Al2O3	63.35	63.55	63.30	62.75	64.29	63.65	64.15	63.61	63.33	64.03	63.63	63.96	63.85	63.72	63.00	63.25	63.22	63.88	63.63	63.93
FeO	0.47	0.35	0.36	0.41	0.48	0.63	0.40	0.71	0.58	0.34	0.24	0.37	0.46	0.56	0.51	0.51	0.43	0.39	0.36	0.30
MnO	0.00	0.00	0.01	0.02	0.02	0.00	0.00	0.01	0.00	0.04	0.01	0.00	0.00	0.01	0.00	0.00	0.00	0.00	0.00	0.03
MgO	0.00	0.00	0.04	0.00	0.04	0.01	0.01	0.02	0.00	0.02	0.01	0.01	0.06	0.07	0.00	0.06	0.03	0.07	0.00	0.00
CaO	0.01	0.00	0.00	0.00	0.01	0.02	0.02	0.00	0.00	0.00	0.00	0.00	0.03	0.02	0.01	0.02	0.00	0.00	0.00	0.01
Na2O	0.00	0.00	0.00	0.00	0.05	0.00	0.00	0.01	0.00	0.00	0.00	0.00	0.05	0.00	0.03	0.00	0.00	0.00	0.00	0.00
K2O	0.00	0.00	0.02	0.02	0.02	0.02	0.01	0.00	0.00	0.01	0.00	0.01	0.00	0.01	0.00	0.01	0.01	0.00	0.00	0.00
Total	100.34	100.34	100.65	99.67	100.90	101.17	101.58	101.32	100.45	101.02	100.41	100.78	101.43	101.04	100.32	101.23	100.83	101.20	101.13	100.97
Numbers of ions on the basis of 20 O																				
Si	3.932	3.923	3.962	3.955	3.859	3.931	3.931	3.941	3.932	3.911	3.925	3.905	3.934	3.920	3.955	3.987	3.974	3.929	3.967	3.928
Ti	0.002	0.003	0.001	0.002	0.001	0.008	0.005	0.006	0.002	0.004	0.004	0.004	0.009	0.005	0.006	0.003	0.005	0.007	0.001	0.001
Al	8.049	8.071	8.014	8.023	8.136	8.027	8.050	8.011	8.041	8.081	8.073	8.091	8.028	8.046	8.007	7.964	7.990	8.047	8.014	8.068
Fe <sup>2+</sup>	0.038	0.028	0.029	0.033	0.039	0.051	0.032	0.057	0.047	0.028	0.020	0.030	0.037	0.045	0.041	0.041	0.035	0.031	0.029	0.024
Mn	0.000	0.000	0.001	0.001	0.002	0.000	0.000	0.001	0.000	0.003	0.001	0.000	0.000	0.001	0.000	0.000	0.000	0.000	0.000	0.003
Mg	0.000	0.000	0.006	0.000	0.006	0.001	0.002	0.004	0.000	0.002	0.001	0.001	0.010	0.010	0.000	0.009	0.005	0.011	0.000	0.000
Ca	0.001	0.000	0.000	0.000	0.002	0.002	0.002	0.000	0.000	0.000	0.000	0.000	0.003	0.002	0.001	0.002	0.000	0.000	0.000	0.002
Na	0.000	0.000	0.000	0.000	0.011	0.000	0.000	0.001	0.000	0.000	0.000	0.000	0.010	0.000	0.006	0.000	0.000	0.000	0.000	0.000
K	0.000	0.000	0.003	0.002	0.003	0.002	0.001	0.000	0.000	0.001	0.000	0.001	0.000	0.001	0.000	0.001	0.001	0.000	0.000	0.000
Total	12.02	12.02	12.02	12.02	12.06	12.02	12.02	12.02	12.02	12.03	12.02	12.03	12.03	12.03	12.02	12.01	12.01	12.03	12.01	12.03

\* pink grains or zone of grains

Table 4

[Click here to download Table: Table 4.xlsx](#)

Tab 4

wt%	V23						V472				V93		
	core	core	int.	int.	int.	rim	core	core	int.	rim	core	int.	rim
SiO <sub>2</sub>	47.20	48.06	47.60	48.05	47.91	47.89	47.60	47.40	48.11	46.92	47.68	47.53	47.48
TiO <sub>2</sub>	bdl	bdl	bdl	bdl	bdl	bdl	bdl	0.02	bdl	bdl	0.01	bdl	0.01
Al <sub>2</sub> O <sub>3</sub>	31.17	31.57	31.92	31.51	31.88	31.75	31.98	31.94	31.97	31.00	31.66	32.14	31.84
FeO	11.52	11.51	11.05	11.17	11.04	11.18	10.89	12.41	9.41	13.53	12.89	12.86	12.81
MnO	0.39	0.38	0.40	0.37	0.39	0.32	0.43	0.65	0.37	0.90	0.43	0.42	0.54
MgO	4.94	5.08	5.10	5.21	5.11	4.96	6.28	5.18	7.12	4.29	5.22	5.21	5.14
CaO	bdl	bdl	0.05	0.04	0.03	0.03	0.03	bdl	0.02	0.01	0.01	0.02	0.03
Na <sub>2</sub> O	1.59	1.55	1.35	1.20	1.20	1.00	0.49	0.57	0.47	0.61	0.63	0.56	0.63
K <sub>2</sub> O	0.01	bdl	0.01	0.03	0.01	0.02	bdl	0.01	bdl	0.02	bdl	0.02	bdl
Total	96.83	98.17	97.47	97.58	98.01	97.14	97.71	98.17	97.48	97.31	98.52	99.03	98.49
Numbers of ions on the basis of 18 O													
Si	5.044	5.058	5.034	5.073	5.054	5.072	5.008	5.004	5.034	5.034	5.022	4.993	5.005
Ti	0.000	0.000	0.000	0.000	0.000	0.000	0.000	0.002	0.000	0.000	0.000	0.000	0.001
Al <sup>IV</sup>	3.928	3.916	3.981	3.923	3.966	3.964	3.966	3.975	3.943	3.922	3.931	3.981	3.958
Sum T	8.972	8.974	9.015	8.996	9.019	9.037	8.973	8.978	8.977	8.956	8.953	8.974	8.962
AlVI	0.000	0.000	0.010	0.000	0.019	0.037	0.000	0.000	0.000	0.000	0.000	0.000	0.000
Fe	1.030	1.013	0.978	0.987	0.974	0.990	0.958	1.096	0.824	1.214	1.136	1.130	1.130
Mn	0.035	0.034	0.036	0.033	0.035	0.028	0.039	0.059	0.033	0.081	0.038	0.038	0.048
Mg	0.788	0.797	0.803	0.820	0.803	0.783	0.984	0.814	1.111	0.687	0.819	0.815	0.807
Sum B	1.852	1.844	1.816	1.840	1.832	1.838	1.981	1.969	1.967	1.982	1.993	1.982	1.985
Ca	0.000	0.000	0.005	0.004	0.004	0.003	0.003	0.000	0.002	0.002	0.001	0.002	0.003
Na	0.329	0.317	0.277	0.247	0.245	0.205	0.100	0.116	0.096	0.128	0.128	0.114	0.130
K	0.001		0.001	0.004	0.002	0.002	0.000	0.002	0.000	0.002	0.000	0.002	0.000
Sum A	0.331	0.317	0.284	0.255	0.251	0.210	0.103	0.118	0.098	0.132	0.129	0.118	0.133
Total	11.155	11.135	11.115	11.091	11.086	11.049	11.058	11.067	11.042	11.070	11.076	11.075	11.081
Fe/(Fe+Mg)	0.57	0.56	0.55	0.55	0.55	0.56	0.49	0.57	0.43	0.64	0.58	0.58	0.58

bdl below detection limit

Table 5

[Click here to download Table: TAB 5.pdf](#)

Run name	Grain/position	Isotope Ratios						Apparent ages					
		Pb207/Pb206	1s	Pb206/U238	1s	Pb207/U235	1s	Pb206/U238	1s	Pb207/U235	1s	Concordia age	2s
Fe23a004	Z1 rim	0,0451	0,0021	0,0025	0,0000	0,0158	0,0007	16	0,3	16	0,7	16	0,6
Fe23a005	Z2 core	0,0720	0,0013	0,1600	0,0025	1,5883	0,0307	957	15	966	19	965	24
Fe23a006	Z3 rim	0,0688	0,0012	0,1441	0,0023	1,3663	0,0269	868	14	875	17	873	23
Fe23a007	Z5 rim	0,0773	0,0037	0,0026	0,0001	0,0272	0,0013	16	0,4	27	1,3	---	---
Fe23a008	Z7 rim	0,0479	0,0022	0,0025	0,0000	0,0167	0,0008	16	0,3	17	0,8	16	0,5
Fe23a009	Z7 core	0,0631	0,0013	0,1152	0,0017	1,0012	0,0218	703	11	704	15	703	19
Fe23a010	Z8 core	0,0997	0,0019	0,2833	0,0044	3,8946	0,0792	1608	25	1613	33	1613	33
Fe23a011	Z10 core	0,0684	0,0012	0,1435	0,0022	1,3532	0,0259	865	13	869	17	868	22
Fe23a012	Z11 core	0,0943	0,0018	0,2616	0,0041	3,4000	0,0689	1498	23	1504	30	1504	32
Fe23a013	Z14 rim	0,0663	0,0013	0,1320	0,0021	1,2068	0,0249	799	13	804	17	802	22
Fe23a014	Z14 rim dark	0,0468	0,0021	0,0024	0,0000	0,0156	0,0007	15	0,3	16	0,7	15	0,5
Fe23a015	Z16 rim dark	0,0514	0,0014	0,0026	0,0000	0,0184	0,0005	17	0,3	19	0,5	---	---
Fe23a016	Z17 rim	0,0564	0,0011	0,0712	0,0011	0,5536	0,0114	444	6,9	447	9,2	445	13
Fe23a017	Z18 rim dark	0,0691	0,0037	0,0028	0,0001	0,0261	0,0014	18	0,4	26	1,4	---	---
Fe23a018	Z18 core	0,0669	0,0012	0,1340	0,0020	1,2354	0,0237	811	12	817	16	814	21
Fe23a019	Z24 rim dark	0,0765	0,0091	0,0028	0,0001	0,0294	0,0034	18	0,5	29	3,4	---	---
Fe23a020	Z24 core	0,0579	0,0018	0,0857	0,0014	0,6840	0,0210	530	8,4	529	16	530	16
Fe23a021	Z26 core dark	0,0474	0,0046	0,0026	0,0001	0,0173	0,0016	17	0,4	17	1,7	17	0,9
Fe23a022	Z28 rim dark	0,0584	0,0012	0,0026	0,0000	0,0212	0,0005	17	0,3	21	0,5	---	---
Fe23a023	Z28 core	0,0809	0,0015	0,1417	0,0022	1,5792	0,0316	854	13	962	19	---	---
Fe23a027	Z30 rim dark	0,0533	0,0015	0,0024	0,0000	0,0172	0,0005	15	0,3	17	0,5	---	---
Fe23a028	Z30 core	0,0556	0,0019	0,0735	0,0012	0,5652	0,0191	457	7,5	455	15	457	14
Fe23a029	Z35 rim dark	0,0714	0,0022	0,0025	0,0000	0,0247	0,0008	16	0,3	25	0,8	---	---
Fe23a030	Z35 core	0,0560	0,0012	0,0679	0,0010	0,5244	0,0114	423	6,4	428	9,3	424	12
Fe23a031	Z37 rim dark	0,0706	0,0017	0,0025	0,0000	0,0244	0,0006	16	0,3	25	0,6	---	---



Table 6

[Click here to download Table: Table 6.xlsx](#)

sample	a)	b)	c)				d)								e)	f)				
	36	XR316	BH14	BH18	BH24	BH10	M3	328B	439	449	450	469	472	473	T117	V471	V91	VS10	VS14	VS38
SiO <sub>2</sub>	72.63	72.40	73.12	73.32	73.67	71.79	71.30	72.65	72.63	73.12	72.23	71.49	72.36	72.72	73.85	76.53	75.37	75.58	74.08	72.67
TiO <sub>2</sub>	0.15	0.31	0.13	0.13	0.13	0.20	0.17	0.15	0.20	0.18	0.20	0.23	0.23	0.22	0.10	0.04	0.038	0.04	0.11	0.18
Al <sub>2</sub> O <sub>3</sub>	14.88	14.81	14.87	14.92	14.86	15.78	15.51	14.68	14.74	14.85	14.96	14.80	14.64	14.89	14.81	14.06	14.13	13.66	14.68	14.91
Fe <sub>2</sub> O <sub>3</sub>	0.89	2.34	0.92	0.93	0.87	1.57	1.68	1.47	1.71	1.49	1.55	1.79	1.77	1.79	1.18	0.58	0.66	0.40	1.17	1.58
MnO	0.02	0.05	0.02	0.01	0.02	0.04	0.03	0.02	0.02	0.02	0.01	0.02	0.02	0.01	0.03	0.01	0.015	0.01	0.03	0.03
MgO	0.78	0.57	0.01	0.08	0.02	0.08	0.34	0.30	0.36	0.33	0.36	0.38	0.38	0.42	0.35	0.12	0.11	0.08	0.19	0.38
CaO	0.88	1.16	0.66	0.66	0.63	0.68	1.03	0.83	0.95	0.78	0.98	0.83	1.02	1.12	0.94	0.51	0.83	0.57	0.83	1.23
Na <sub>2</sub> O	3.68	3.74	3.91	4.10	4.04	3.59	4.00	3.34	3.59	3.72	3.73	3.72	3.64	3.54	3.34	3.89	3.3	2.99	3.04	3.45
K <sub>2</sub> O	4.91	4.08	4.97	4.82	4.76	5.20	4.89	5.42	4.86	4.55	4.57	4.53	4.49	4.58	4.36	3.32	4.62	5.91	4.86	4.37
P <sub>2</sub> O <sub>5</sub>	0.12	0.04	0.09	0.14	0.10	0.07	0.14	0.12	0.14	0.16	0.13	0.13	0.11	0.09	0.19	0.15	0.1	0.14	0.10	0.14
LOI	0.70	0.62	1.43	0.98	1.01	0.89	0.76	0.81	0.83	0.91	0.79	1.78	0.73	0.84	0.80	0.69	0.83	0.50	0.80	0.90
Total	99.64	100.13	100.14	100.10	100.12	99.90	99.86	99.80	100.04	100.12	99.52	99.71	99.40	100.23	99.95	99.91	100.01	99.88	99.89	99.84
ASI	1.15	1.17	1.14	1.13	1.15	1.24	1.13	1.14	1.14	1.19	1.16	1.18	1.15	1.16	1.24	1.29	1.18	1.11	1.25	1.18
Q	35	39	33	33	34	34	28	34	36	37	36	36	37	37	41	44	41	37	41	39
Or	30	24	31	30	29	32	27	35	29	28	28	28	27	28	27	20	29	36	30	27
Ab	35	38	36	38	37	34	34	31	35	36	36	37	36	35	32	36	31	27	29	34
sill					X		X	X					X						X	X
cord							X	X	X				X						X	X
TZrn °C							742	734	734	741	739	736	739	746	708	647	690	670	760	744
TREE °C							781	767	781	781	—	—	782	798	738	683	701	681	790	797